

Computational and Experimental Study of the Mechanics of Embryonic Wound Healing

Matthew A. Wyczalkowski^{a,1,*}, Victor D. Varner^b, Larry A. Taber^a

^a*Department of Biomedical Engineering, Washington University, St. Louis, MO 63130*

^b*Department of Chemical and Biological Engineering, Princeton University, Princeton, NJ 08544*

Abstract

Wounds in the embryo show a remarkable ability to heal quickly without leaving a scar. Previous studies have found that an actomyosin ring (“purse string”) forms around the wound perimeter and contracts to close the wound over the course of several dozens of minutes. Here, we report experiments that reveal an even faster mechanism which remarkably closes wounds by more than 50% within the first 30 seconds. Circular and elliptical wounds ($\sim 100 \mu\text{m}$ in size) were made in the blastoderm of early chick embryos and allowed to heal, with wound area and shape characterized as functions of time. The closure rate displayed a biphasic behavior, with rapid constriction lasting about a minute, followed by a period of more gradual closure to complete healing. Fluorescent staining suggests that both healing phases are driven by actomyosin contraction, with relatively rapid contraction of fibers at cell borders within a relatively thick ring of tissue (several cells wide) around the wound followed by slower contraction of a thin supracellular actomyosin ring along the margin, consistent with a purse string mechanism. Finite-element modeling showed that this idea is biophysically plausible, with relatively isotropic contraction within the thick ring giving way to tangential contraction in the thin ring. In addition, consistent with experimental results, simulated elliptical wounds heal with little change in aspect ratio, and decreased membrane tension can cause these wounds to open briefly before going on to heal. These results provide new insight into the healing mechanism in embryonic epithelia.

Keywords: biomechanics, chick embryo, epithelium, finite elements, epithelial morphogenesis, mechanobiology, growth

*Corresponding Author

¹Current address: The Genome Institute, Washington University, St. Louis, Missouri 63108, USA

1. Introduction

Embryonic epithelia display a remarkable ability to repair wounds, and use a series of redundant mechanisms to do so. Shortly after a wound is made, an actomyosin cable forms at the wound edge and contracts, drawing the wound closed by a purse string mechanism (Jacinto et al., 2001; Martin and Lewis, 1992; Redd et al., 2004). Filopodia and lamellipodia also frequently form to draw in apposing edges like a zipper (Jacinto et al., 2000; Wood et al., 2002). Both these mechanisms require the polymerization of new actin structures that can form relatively quickly, over a period of minutes. Here, we report on a cell contraction mechanism that precedes these other mechanisms and operates on an even faster time scale. To our knowledge, this rapid healing phase has not been studied previously. Together, these mechanisms (fast contraction, slow contraction, zippering) constitute three phases for embryonic wound healing.

Much of the cellular machinery used in wound healing also is used during morphogenesis (Martin and Parkhurst, 2004; Sonnemann and Bement, 2011; Wood et al., 2002). In *Drosophila* dorsal closure, for example, two epithelial sheets are drawn together and fuse in a process remarkably similar to the healing of embryonic wounds, with both the purse string and zippering mechanisms playing a significant role (Hutson et al., 2003). The mechanisms of embryonic wound healing are significantly different from adult wounds, which tend to involve crawling fibroblasts and an inflammatory response that can lead to scarring. Embryonic wounds, by contrast, heal relatively quickly and do not form scars, and thus may offer clinical insight to improving adult wound healing (Redd et al., 2004; Sonnemann and Bement, 2011).

The mechanics of wound healing are herein studied in the blastoderm of early chick embryos. We found that the rapid healing phase partly closes the wound within tens of seconds, followed by the slower healing phase which continues over the course of minutes. Using fluorescence microscopy and finite-element modeling to characterize the healing mechanisms, we found that the unexpectedly rapid and previously uncharacterized initial healing phase is driven by an approximately isotropic contraction of cells within a relatively thick ring around the wound. Subsequent assembly and contraction of an actomyosin cable (“purse string”) accounts for the second, slower phase, and these two mechanisms are able to account for the observed behavior in the first ten minutes of wound healing. Filopodial zippering constitutes the third phase, which is not incorporated into our model.

2. Background

The chick embryo has been a popular model for studies of wound healing (Bortier et al., 1993; Brock et al., 1996; England and Cowper, 1977; Lawson and England, 1998; Mareel and Vakaet, 1977; Martin and Lewis, 1992; Stanisstreet et al., 1980). The early embryo consists of a planar blastoderm, two to three cell layers thick, which is held under tension and attached to a substrate (the vitelline membrane) only at its periphery (Bellairs et al., 1967; Bortier et al., 1993; New, 1959). All forces required to close a wound are generated within the blastoderm itself.

A critical initial signal of a wounding event is the influx of extracellular calcium (Ca^{2+}) into the perforated cells, as well as its release from intracellular stores (Benink and Bement, 2005; Cordeiro and Jacinto, 2013; Woolley and Martin, 2000; Xu and Chisholm, 2011). Among other roles, Ca^{2+} triggers a signaling cascade involving small GTPase molecules which play a central and necessary role in the regulation of wound healing, including recruitment of actin and myosin to the wound edge, actomyosin assembly and contraction, and the formation of filopodia (Bement

et al., 2006; Brock et al., 1996; Clark et al., 2009; Sonnemann and Bement, 2011; Wood et al., 2002). A number of different wound healing mechanisms occur in various model organisms. Actomyosin purse strings are widely observed in both single-cell and multicellular wounds (Clark et al., 2009; Kiehart, 1999; Martin and Lewis, 1992). Epithelial cells crawling over a mesenchymal substrate (Radice, 1980), as well as contraction of the substrate itself (Davidson et al., 2002; McCluskey and Martin, 1995), can also help close embryonic wounds. In the present study, however, the wounds were cut completely through the blastoderm, and there is no substrate to aid healing.

Published work on the healing of elliptical-shaped embryonic wounds is inconclusive on how the shape of the wound changes as it heals. Elongated wounds in *Drosophila* embryos maintain an approximately constant aspect ratio (AR) as they close (Hutson et al., 2003). Small elliptical wounds in *Xenopus* oocytes (frog eggs) round as they heal (Mandato and Bement, 2001). Larger, superficial rectangular wounds in multicellular *Xenopus* embryos with an underlying mesenchyme, however, become more elongated during healing (Davidson et al., 2002).

In contrast to wound healing in adult tissue, which operates by markedly different processes, modeling of embryonic wound healing has received relatively little attention (Murray, 2003; Olsen et al., 1995; Wyczalkowski et al., 2012). Much of the published work is based on the mechanochemical model of Murray and Oster (1984) for the morphogenesis of epithelial sheets. Sherratt et al. (1992) (see also Murray 2003) considered the quasi-static response of such a sheet to wounding, and Sadvovsky and Wan (2007) extended this model to incorporate wound closure. Previously we presented a model for a circular wound in which the healing response is governed by a stretch-activated morphomechanical feedback law (Taber, 2009). Nagai and Honda (2009) developed a vertex dynamics model where minimization of interfacial energy leads to the closing of a wound. Finally, Hutson et al. (2003) (see also Layton et al. 2009) developed a model incorporating an actomyosin ring and filopodial zippering for the related problem of dorsal closure in *Drosophila*.

Tissue-scale deformations are driven by cell division, cell intercalation, cytoskeletal contraction, or some combination of these and other processes. The present analysis is based on our tissue-level theory for epithelial morphogenesis (Taber, 2009), in which these processes are simulated by active changes in the local zero-stress configuration. The kinematic equations of continuum mechanics are modified to include volumetric growth (Rodriguez et al., 1994), which has been used to effectively simulate a number of morphogenetic processes (Muñoz et al., 2007; Taber, 2009; Varner et al., 2010; Ambrosi et al., 2011; Filas et al., 2012). Here, we consider only active contraction of tissue, as simulated by negative growth, and do not consider the contributions of filopodia.

3. Experimental Methods

3.1. Embryo Preparation and Culture

Fertilized white Leghorn chicken eggs were incubated at 37°C for 20-22 hours (of a 21-day incubation period) in a humidified, forced draft incubator to yield embryos at approximately Hamburger-Hamilton (HH) stage 4 (Hamburger and Hamilton, 1951). Whole embryos were harvested from the eggs using a filter paper carrier method (Voronov and Taber, 2002) which preserves the stresses normally present in the tissue.

At this early stage of development, the embryonic blastoderm is organized as a nearly flat sheet in a state of approximately uniform, isotropic tension (Varner et al., 2010) (Fig. 1a). The blastoderm is connected to the vitelline membrane only at its outer periphery, and consists of two epithelial cell layers, the endoderm and ectoderm. A third cell layer, the mesoderm, consists of

migratory mesenchymal cells and spreads between the endoderm and ectoderm, although at this stage of development its extent is limited (Bortier et al., 1993; England and Wakely, 1977). While the endoderm and ectoderm have important differences, wounds passing through both layers heal in the same manner as ectoderm-only wounds (Stanisstreet et al., 1980). Insofar as we can tell the germ layers do not move significantly with respect to one another during healing, and we do not distinguish between the layers.

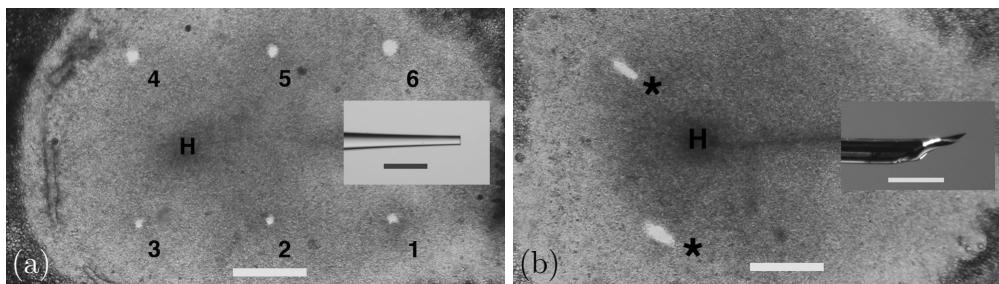


Figure 1: Early stage (HH4) chick embryos with circular and elliptical wounds, ventral side up and anterior to the left. Hensen’s node marked by “H”. Scale bars $500\mu\text{m}$. (a) Circular wounds (numbered 1-6) several seconds after being created with a circular punch (inset). (b) Two elliptical wounds (indicated by *) created with microscalpel (inset).

After harvesting, embryos were placed atop a 2% agar/98% phosphate buffered saline (PBS) gel in Delta T Dishes (Bioprotechs, Butler, PA), submerged under a thin layer of liquid culture media (Voronov and Taber, 2002), and incubated for at least one hour. Prior to wounding, the embryos were removed from the incubation chamber and allowed to equilibrate in the Delta T4 Culture Dish Controller under the same incubation conditions.

3.2. Wounding and Imaging

Circular and linear incision wounds were cut completely through the blastoderm. For dynamic imaging we created between 1 and 6 circular wounds per embryo, positioned as illustrated in Fig. 1a for a representative embryo. Elliptical wounds, as well as circular wounds used for fluorescence imaging, were created in pairs and positioned anterior and lateral to Hensen’s node (as in Fig. 1b), where the mesoderm is absent (England and Wakely, 1977). The location of the wounds generally did not affect their behavior.

To create circular wounds, a microforged glass micropipette ($42\mu\text{m}$ inner, $57\mu\text{m}$ outer radii) held in a micromanipulator was used to punch through the blastoderm and excise circular plugs of tissue of uniform size (Fig. 1a)(Varner and Taber, 2010). Linear incisions approximately $200\mu\text{m}$ in length were made by drawing a handheld microscalpel (Conrad et al., 1993) across the blastoderm surface. Tension in the membrane caused these wounds to open into an initial elliptical shape (Fig. 1b). In both cases, wounds were concealed by the wounding apparatus while they were made, with the first unobscured frame visible 2-4 seconds after wounding.

Wounds were created and allowed to heal under incubation conditions, and were observed for the entire duration of the experiment by a combination of video and still digital imaging. Wound area was determined by thresholding using ImageJ (Abràmoff et al., 2004), with the threshold value selected to isolate the bright wound from the darker surrounding tissue. While somewhat subjective, variations in the threshold value resulted in relatively small changes in the calculated

wound radii and do not significantly affect the results presented here. Manual correction of wound shape was performed in a few elliptical wound cases where debris temporarily impinged upon the wound area. The ratio of major to minor radius of elliptical wounds (the wound aspect ratio, AR) was obtained by fitting the isolated wound shape with an ellipse of equivalent area and second moment of inertia.

Fluorescence staining was used to visualize the actin cytoskeleton and phosphorylated myosin II light chain (pMLC), as described previously (Filas et al., 2012). Wounded embryos were fixed at a given time after wounding by injecting 37% formaldehyde into the media at a 1:10 volume ratio. F-actin was visualized with rhodamine phalloidin, while immunofluorescence staining was used for pMLC. Following staining, the endoderm and ectoderm in the vicinity of the wound were separated using drawn glass capillary tube needles. Small pieces of both germ layers were then excised and mounted for fluorescence imaging.

4. Experimental Results

We analyzed 52 circular wounds from 15 embryos and 13 elliptical wounds from 10 embryos. We discarded embryos due to blastoderm detachment, excessive floating debris, or other experimental problems; we also discarded a minority of wounds which never healed. Of those analyzed, nearly all (62/65) closed relatively quickly and typically healed fully within ten minutes to two hours, depending on wound size as well as wound location and stage of embryonic development. Three circular wounds initially closed partly, then expanded for several minutes before going on to heal. Relatively wide variations in healing time for such wounds have been previously reported (Stanisstreet et al., 1980).

Our analysis focuses on the first ten minutes after wounding. Most of the healing, as measured by wound area, took place during this time, and optical characterization of wound area and shape is most reliable during this period, as discussed below. Subsequent modeling focuses on this time period as well.

4.1. Circular Wound Area

The experimental wound area is shown as a function of time after wounding for six circular wounds (Fig. 2 and *Supplemental Video 1*). Immediately after formation, wound area decreased rapidly for about 30 seconds. After this period the wounds continued to close, but significantly more slowly. To minimize variability from differing experimental conditions and embryos and to facilitate quantitative statistics, we consider here only wounds from a single embryo (shown in Fig. 1a). However, the qualitative behavior shown in Fig. 2 is representative of that observed in nearly all embryos we analyzed; in particular, wounds broadly displayed distinct fast and slow phases of healing.

Nonlinear regression indicated that a single exponential cannot adequately account for the observed healing behavior, and we approximate the area versus time relationship for each of the wounds in Fig. 2 using a double exponential function of the form

$$a(t) = c_0 + c_1 \exp(-t/T_1) + c_2 \exp(-t/T_2), \quad (1)$$

which contains two characteristic time constants, T_1 and T_2 . Choosing $T_1 < T_2$, we identify c_1 and c_2 as the magnitudes of the fast and slow phases of wound healing, respectively. For each wound we used nonlinear least squares fitting to obtain values for each of the five parameters in Eq. (1)

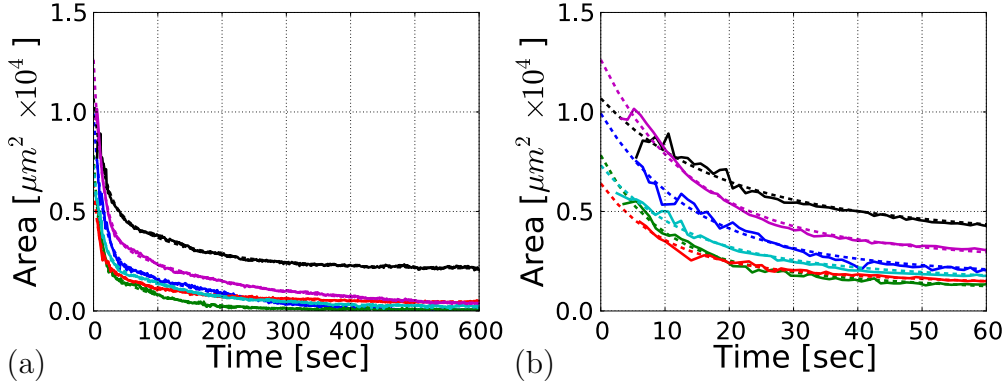


Figure 2: Experimental wound area vs. time for circular wounds. Experimental data (solid curves) are for six wounds from a single representative embryo (pictured in Fig. 1a). Dashed curves indicate best fit of Eq. (1) for each wound (parameter values in Table S1). Panels a, b show the first 10 minutes and 1 minute of wound healing, respectively. Good fit to data obscures dashed curves in panel a.

(listed in Table S1). The dashed curves in Fig. 2 show the resulting fit, illustrating that the double exponential function reproduces trends in the data quite well.

For all six wounds the fast phase is responsible for the bulk of the decrease in wound area ($c_1 \sim 2c_2$), and the associated time constant is $T_1 = 12.4 \pm 2.5$ sec. The time constant of the slow phase is more variable, but is generally ten or more times greater than T_1 ($T_2 = 140 \pm 40$ sec). We used the mean parameters T_i and c_i (Table S1) to construct a mean wound response. Not all wounds closed within ten minutes, an aspect which is captured by the c_0 term, and which accounts for the large variation in c_0 . Evaluating Eq. (1) for $t = 0$ with the mean wound parameters yields the reference wound area $a_0 = 9130 \mu\text{m}^2$, corresponding to a radius $r_w = 54 \mu\text{m}$. This initial wound size is intermediate between the pipette inner and outer radii (42 and 57 μm , respectively). This observation is consistent with previous reports which indicate that the inner radius of the pipette is the cutting edge Varner and Taber (2010). Once cut, the wound edge then recoils due to blastoderm tension.

The relatively large difference between the time constants T_1 and T_2 suggests that there are (at least) two distinct physical mechanisms operating to close the wound during the first ten minutes. The initial phase, associated with time constant T_1 , results in the bulk of wound closing within ~ 20 – 30 seconds of wounding (area at 30 seconds is 35% a_0). This is followed by a second phase, associated with T_2 , which operates more slowly to close the wound the rest of the way. The second healing phase appears consistent with actomyosin cable assembly and contraction, with a time scale in line with published work on the dynamics of actin cable formation (Abreu-Blanco et al., 2011; Brock et al., 1996; Clark et al., 2009). As discussed later, however, the rate of the initial mechanism appears too rapid for *de novo* actomyosin assembly. Filopodial zippering appears to play an insignificant role at this time scale.

4.2. Elliptical Wound Area and Shape

Following linear cuts, wounds opened into elliptical shapes as quickly as could be observed. The area and AR of five representative elliptical wounds, all from different embryos, are plotted in Figure 3. The initial areas and aspect ratio trends of the elliptical wounds are more variable than the circular ones, in part because they are from different embryos and wound size is somewhat less

repeatable. Consequently, we restrict ourselves here to a qualitative description of elliptical wound healing.

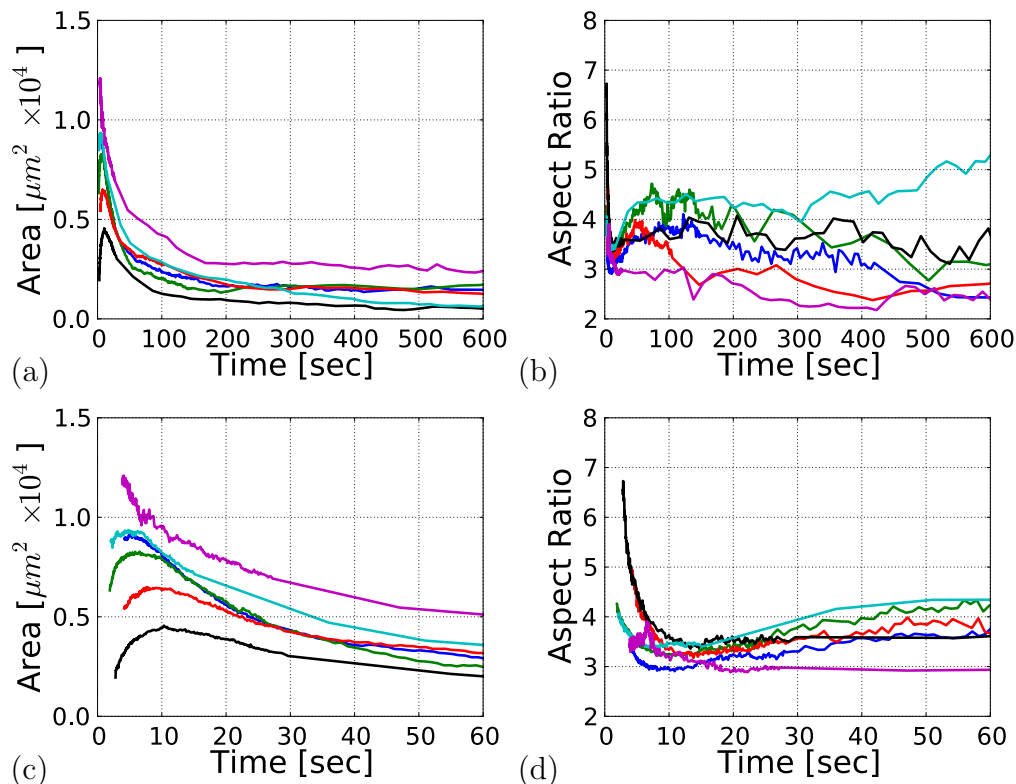


Figure 3: Experimental wound area and aspect ratio (AR) vs. time for elliptical wounds. Each wound is from a different embryo. (a, b) Area and AR, respectively, for ten minutes post wounding. (c, d) The same quantities for the first minute. Sampling rate changes correspond to transition from video to still image acquisition (see Sec. 3.2).

Like circular lesions, elliptical wounds closed at a rapid initial rate, then more gradually until fully healed. For some wounds the area initially increased for several seconds before decreasing, although this was not observed in all elliptical wounds (Figs. 3a,c). No circular wounds displayed such transient gaping behavior.

Figures 3b,d show the AR of healing elliptical wounds. The AR, obtained from the quotient of two fluctuating quantities, is subject to large fluctuations, particularly as wounds become small (see also Section 7.2.3). Nevertheless, it is clear the AR tends to stay relatively constant, indicating that the wounds neither round up ($\text{AR} \rightarrow 1$) nor become slit-like ($\text{AR} \rightarrow \infty$) as they heal. Notably, in cases where the area of the wound transiently increases immediately after wounding, there is a corresponding initial decrease in the AR.

We reason that, since the same chemo-mechanical processes are involved for both circular and elliptical wound healing, differences in their behavior (e.g., initial increase in area) are likely caused by geometric effects, a topic we address in Section 7.3.

4.3. Actin and Myosin Staining

To obtain clues concerning the origin of the forces that close the wounds, we investigated the distributions of F-actin and activated myosin (pMLC) at various times after wounding. To visualize actin distribution more clearly, we separated the two epithelial monolayers, endoderm and ectoderm, and imaged them separately (Fig. 4). These layers display different cell morphologies, with the thicker ectoderm consisting of columnar epithelial cells and the thinner endoderm of squamous cells (Bellairs and Osmond, 2005; England and Lawson, 1993). Nevertheless, the conclusions drawn here regarding their healing response are broadly similar.

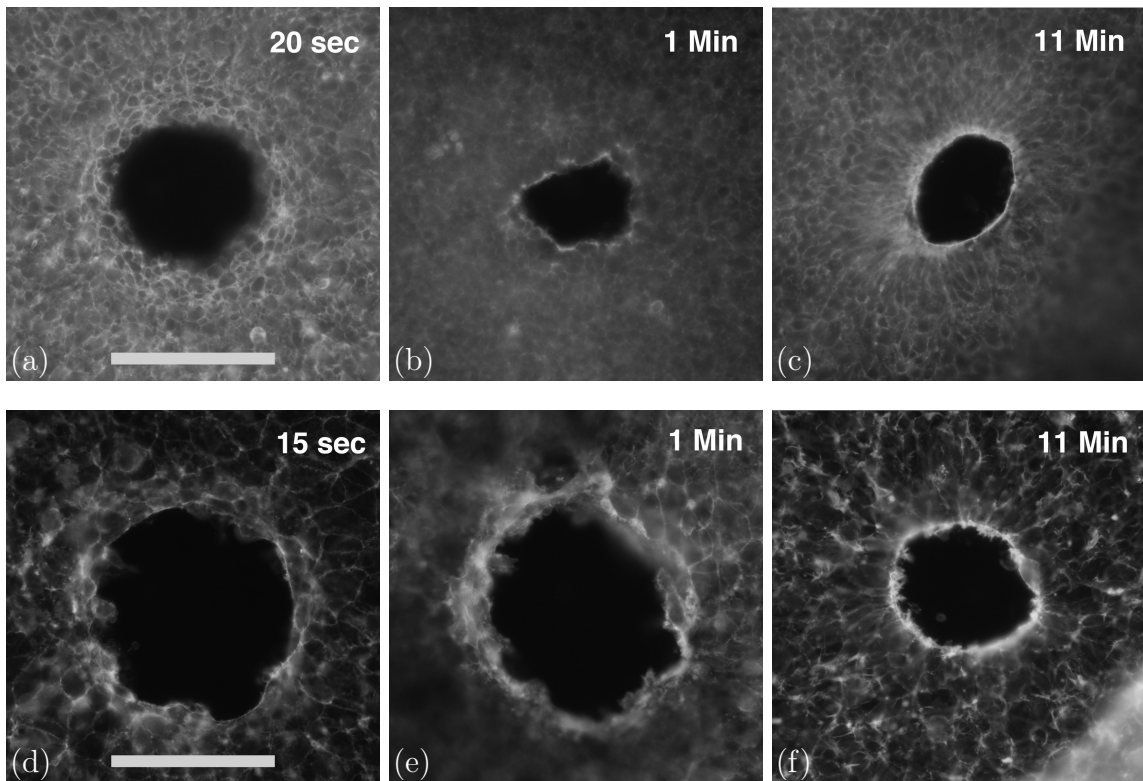


Figure 4: Fluorescence images of circular wounds stained for actin at given times after wounding. (a–c) ectoderm; (d–f) endoderm. Scale bars $100\mu\text{m}$. Panels a and d are from different embryos, while b and e are same wound, and c and f are same wound.

Tens of seconds after wounding, we observed a broad, diffuse ring of enhanced actin fluorescence near the wound in both the ectoderm (Fig. 4a) and the endoderm (Fig. 4d). This intensified fluorescence, an indicator of increased F-actin localization, coincided mainly with cell borders. A minute or so after wounding this ring had largely dissipated, except at the wound border where the stain became more intense (Figs. 4b,e, see also Fig. S3). By ten minutes actin had formed a continuous, distinct supracellular structure along the wound border, characteristic of an actomyosin cable (Figs. 4c,f). For convenience, we denote the initial and subsequent actin regions as the “thick ring” and “thin ring,” respectively. In addition to the cable structure, finger-like filopodia and leaf-like lamellipodia were seen in the endoderm (Figs. 4e, S1), consistent with previous reports (see Section 7.2.3).

While the boundary of the thick ring was not sharply defined and its precise size and timing of disappearance were variable (Figs. 4a, S3), it was roughly $40 \mu\text{m}$ in width and of comparable size around both circular and elliptical wounds (data not shown). The width of the thin ring was also variable but generally $1\text{-}3 \mu\text{m}$ wide, consistent with published reports (Martin and Lewis, 1992).

To better establish the correlation between actin fluorescence intensity and mechanical force production, we also stained circular wounds for phosphorylated myosin II light chain (pMLC), which is the activated conformation of the myosin molecule (Lecuit et al., 2011). The results (Fig. S2) show essentially the same features as actin staining, with a thick ring around the wound immediately after wounding and a sharp, condensed cable structure ten minutes later.

These results suggest that the initial phase of wound healing, associated with the time constant T_1 , is driven by rapid cellular contraction within a thick ring of cells around the wound. The second phase, associated with the time constant T_2 , is in turn driven by slower contraction of a relatively thin actomyosin cable.

5. Computational Model for Wound Healing

To investigate the plausibility of our proposed healing mechanisms, we constructed a finite-element model that incorporates active tissue contraction. The blastoderm is modeled as an initially homogeneous single-layered membrane in plane stress under isotropic tension σ_B (Fig. 5a). The material properties associated with this epithelial membrane capture the collective mechanical contributions of both the endoderm and ectoderm, including cellular cytoplasm and cortical actin. From our experimental results, we propose that wounding triggers two distinct mechanisms: (1) initial contraction of cells in a thick ring surrounding the wound, and (2) subsequent assembly and contraction of actomyosin fibers in a thin ring at the wound border.

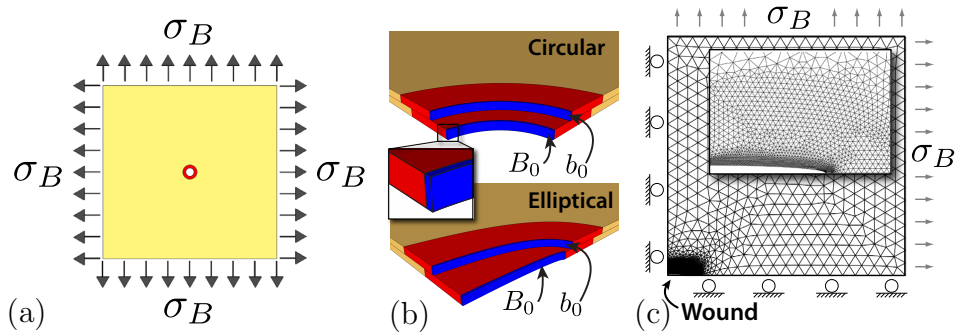


Figure 5: Schematic of model. (a) Geometry of circular wound model in reference configuration b_0 . The blastoderm is modeled as a square single-layered epithelial membrane under isotropic tension σ_B with a centered wound. (b) Detail of wound region for circular and elliptical wounds. The thick (cell) ring is shown in red, and the thin (fiber) ring in blue. The layers indicate the geometry in the undeformed (B_0) and reference (b_0) configurations, illustrating differences resulting from applied boundary stress: tension σ_B enlarges the wound and, in the elliptical case, decreases the AR. Inset illustrates relative width of thin ring (see also Fig. 12) (c) Finite-element model detail, illustrating the mesh in the B_0 configuration for the elliptical wound (circular wound is similar). Roller boundary conditions on two internal edges enforce quarter-symmetry conditions, outer edges have a specified stress σ_B , and wound edges are stress-free. Inset details the wound region.

To incorporate these mechanisms into our model, the membrane is treated as a constrained pseudo-elastic mixture consisting of two contractile components: “cells” and “fibers” (Humphrey and Rajagopal, 2002). Immediately after wounding, cells contract within the thick ring (red area, Fig. 5), while contractile fibers form more gradually in the thin ring, replacing cells in the process (blue area, Fig. 5). The fibers are assumed to be stiffer than cells, created in a prestretched configuration, and to contract along their length. Working together, cell contraction, assembly of prestretched fibers, and subsequent fiber contraction generate the mechanical forces that close the wound. Both circular and elliptical wounds are considered in our model (see Appendix A for geometric considerations).

In our model, active contraction is simulated as negative growth using the theory of Rodriguez et al. (1994) for finite volumetric growth (Ramasubramanian et al., 2006; Ramasubramanian and Taber, 2008). As in theories for thermoelasticity and elastoplasticity (Lubarda, 2004), the total deformation gradient tensor is decomposed into elastic deformation and active growth tensors. This theory is compatible with fundamental thermodynamic principles (Lubarda and Hoger, 2002; Menzel and Kuhl, 2012). We consider herein two models for fiber formation. First, we discuss the “multiple fiber” model, which is based on the constrained mixture and evolving natural configurations theory of Humphrey and Rajagopal (2002). Next, we describe a simpler “single fiber” model, which is a special case of the multiple fiber model and offers numerical efficiency.

5.1. Kinematic Equations

\mathbf{G}^i	Cell/fiber growth tensor
\mathbf{F}^{i*}	Cell/fiber elastic deformation gradient tensor
\mathbf{F}_0^{f*}	Fiber pre-stretch tensor
\mathbf{F}	Total deformation gradient tensor of body (cell and fiber)
\mathbf{C}^{i*}	Right Cauchy-Green elastic deformation tensor
$\boldsymbol{\sigma}^i$	Cell/fiber Cauchy stress tensor
λ^{f*}	Fiber elastic stretch ratio
ϕ^i	Cell/fiber volume fraction
J^{i*}	Cell/fiber elastic volume ratio
W^i	Cell/fiber strain-energy density function
τ_j	Intermediate time $0 \leq \tau_j \leq t$ of virtual configuration
I_1^*, I_3^*	Cell strain invariants
G^i	Scalar cell/fiber growth measure

Table 1: Nomenclature definitions. Superscript $i = c$ for cells, $i = f$ for fibers.

Applied equibiaxial tension σ_B initially deforms the stress-free membrane B_0 into the reference configuration b_0 (Fig. 5b). With σ_B held constant, contraction is then specified as a function of position and time for $t > 0$. The theory behind the present work is described below; further details can be found in previous reports on the mechanics of growth and morphogenesis (Rodriguez et al., 1994; Taber, 2001).

Following the creation of a wound, cells in the thick ring begin to contract while actin and myosin are recruited to the wound periphery (Sonnemann and Bement, 2011), where they assemble into a thin supracellular cable that contracts over the course of minutes (Fig. 4). As individual actomyosin fibers incorporate into the cable over time, they each experience a different mechanical environment due to the ongoing deformation of the tissue. To model this behavior, each fiber is assumed to form at an intermediate time τ and subsequently contract.

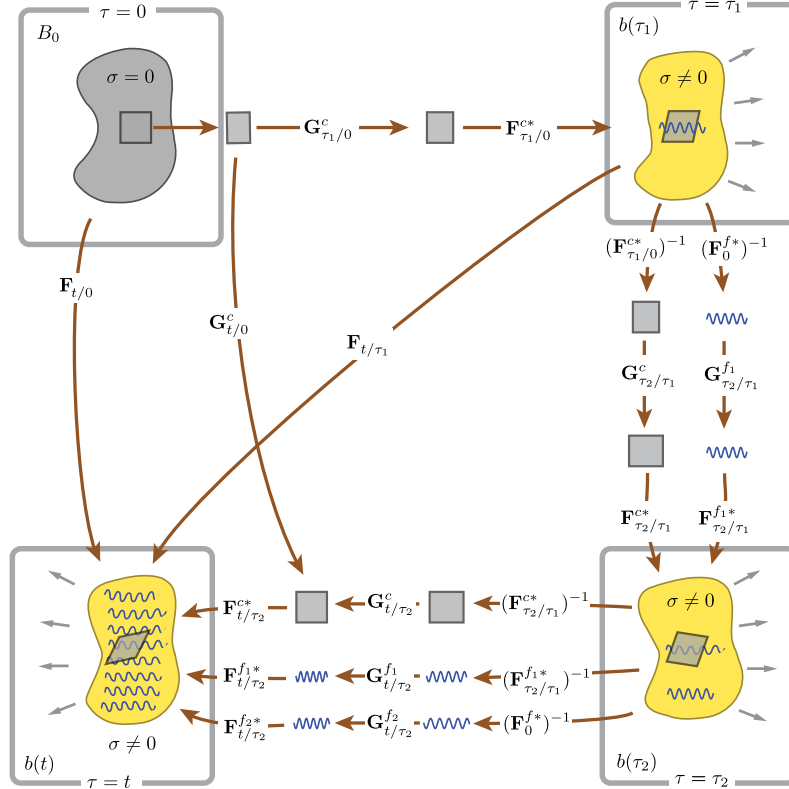


Figure 6: Sequence of configurations which transform unloaded body B_0 into current configuration $b(t)$, with fibers created at some intermediate time τ . See Table 1 for definitions. The mapping of the total deformation between times τ_i and τ_j is given by $\mathbf{F}_{\tau_j/\tau_i}$, while $\mathbf{G}_{\tau_j/\tau_i}^c$ and $\mathbf{F}_{\tau_j/\tau_i}^{c*}$ give the corresponding contraction and elastic deformation, respectively. The contraction and elastic deformation of cells and each of the fibers is considered individually, but all components, once created, undergo the same total deformation. The reference configuration $b(0)$ is a special case of $b(t)$, with no growth ($\mathbf{G}^i = \mathbf{I}$) and only surface loads contributing to deformation.

In the scheme illustrated in Figure 6, the first group of fibers is created at time τ_1 (see Table 1). Before this time, each cell in B_0 contracts to a new zero-stress state defined by the contraction (growth) tensor $\mathbf{G}_{\tau_1/0}^c$, which generally varies with time and space. The cell then deforms through the elastic deformation gradient tensor $\mathbf{F}_{\tau_1/0}^{c*}$. This deformation is caused by surface loads, as well as by geometric compatibility requirements when the cells are reassembled into the intermediate configuration $b(\tau_1)$. Fibers are created in $b(\tau_1)$ at a prestretch \mathbf{F}_0^{f*} relative to their own zero-stress state. Here, we assume that \mathbf{F}_0^{f*} is the same for all fibers.

Thereafter these newly created fibers are constrained to undergo the same total deformation pointwise as the cells. For the time scale considered here, we assume that fiber degradation is negligible. During the interval from τ_1 until the next group of fibers form at τ_2 , the cells contract by $\mathbf{G}_{\tau_2/\tau_1}^c$, while the fibers contract by $\mathbf{G}_{\tau_2/\tau_1}^{f_1}$ relative to their individual zero-stress configurations, with the label f_1 indicating the fiber under consideration. The zero-stress configurations at τ_1 are obtained by reversing the elastic deformations in $b(\tau_1)$ of both cells ($\mathbf{F}_{\tau_1/0}^{c*}$) and fibers (\mathbf{F}_0^{f*}). The cells and fibers then undergo elastic deformations $\mathbf{F}_{\tau_2/\tau_1}^{c*}$ and $\mathbf{F}_{\tau_2/\tau_1}^{f_1*}$, respectively, to give the body $b(\tau_2)$ in which the second set of fibers form. This scheme continues until the current configuration $b(t)$. In general, we may write for cells ($i = c$) and fibers ($i = f$) $\mathbf{F}_{t/0}^i = \mathbf{F}_{t/\tau}^i \cdot \mathbf{F}_{\tau/0}^i$ and $\mathbf{G}_{t/0}^i = \mathbf{G}_{t/\tau}^i \cdot \mathbf{G}_{\tau/0}^i$. This decomposition does not hold, however, for the elastic deformation, i.e., $\mathbf{F}_{t/0}^{i*} \neq \mathbf{F}_{t/\tau}^{i*} \cdot \mathbf{F}_{\tau/0}^{i*}$. For a constrained mixture, the deformation of the fibers, once formed, is identical to the deformation of the cells and the composite body as a whole, i.e., $\mathbf{F}_{t/\tau}^f = \mathbf{F}_{t/\tau}^c = \mathbf{F}_{t/\tau}$, where we write $\mathbf{F}_{t/\tau}^f = \mathbf{F}_{t/\tau}^{f_i}$ as the total deformation at t for fibers created at time τ .

The total deformation gradient tensor $\mathbf{F}_{t/0}$ maps the undeformed configuration B_0 into the current configuration $b(t)$. For cells, the sequence of transformations which together compose $\mathbf{F}_{t/0}^c = \mathbf{F}_{t/0}$ is given by (Figure 6)

$$\begin{aligned} \mathbf{F}_{t/0}^c &= \mathbf{F}_{t/\tau_2}^{c*} \cdot \mathbf{G}_{t/\tau_2}^c \cdot (\mathbf{F}_{\tau_2/\tau_1}^{c*})^{-1} \cdot \mathbf{F}_{\tau_2/\tau_1}^{c*} \cdot \mathbf{G}_{\tau_2/\tau_1}^c \cdot (\mathbf{F}_{\tau_1/0}^{c*})^{-1} \cdot \mathbf{F}_{\tau_1/0}^{c*} \cdot \mathbf{G}_{\tau_1/0}^c \\ &= \mathbf{F}_{t/\tau_2}^{c*} \cdot \mathbf{G}_{t/\tau_2}^c \cdot \mathbf{G}_{\tau_2/\tau_1}^c \cdot \mathbf{G}_{\tau_1/0}^c \\ &= \mathbf{F}_{t/\tau_2}^{c*} \cdot \mathbf{G}_{t/0}^c, \end{aligned} \quad (2)$$

where $\mathbf{G}_{t/0}^c \equiv \mathbf{G}_{t/\tau_2}^c \cdot \mathbf{G}_{\tau_2/\tau_1}^c \cdot \mathbf{G}_{\tau_1/0}^c$. This equation gives the elastic cell deformation as

$$\mathbf{F}_{t/\tau_2}^{c*} = \mathbf{F}_{t/0}^c \cdot (\mathbf{G}_{t/0}^c)^{-1} = \mathbf{F}_t^{c*}, \quad (3)$$

where we write $\mathbf{F}_{t/\tau_2}^{c*} = \mathbf{F}_t^{c*}$ since the cell elastic deformation is independent of the fiber creation time τ .

For fibers created at τ_1 , the total deformation $\mathbf{F}_{t/\tau_1}^f = \mathbf{F}_{t/\tau_1}$ is (see Fig. 6)

$$\begin{aligned} \mathbf{F}_{t/\tau_1}^f &= \mathbf{F}_{t/\tau_2}^{f_1*} \cdot \mathbf{G}_{t/\tau_2}^{f_1} \cdot (\mathbf{F}_{\tau_2/\tau_1}^{f_1*})^{-1} \cdot \mathbf{F}_{\tau_2/\tau_1}^{f_1*} \cdot \mathbf{G}_{\tau_2/\tau_1}^{f_1} \cdot (\mathbf{F}_0^{f_1*})^{-1} \\ &= \mathbf{F}_{t/\tau_2}^{f_1*} \cdot \mathbf{G}_{t/\tau_2}^{f_1} \cdot \mathbf{G}_{\tau_2/\tau_1}^{f_1} \cdot (\mathbf{F}_0^{f_1*})^{-1} \\ &= \mathbf{F}_{t/\tau_2}^{f_1*} \cdot \mathbf{G}_{t/\tau_1}^{f_1} \cdot (\mathbf{F}_0^{f_1*})^{-1}, \end{aligned} \quad (4)$$

with $\mathbf{G}_{t/\tau_1}^{f_1} = \mathbf{G}_{t/\tau_2}^{f_1} \cdot \mathbf{G}_{\tau_2/\tau_1}^{f_1}$. Solving for the elastic deformation of fibers created at τ_1 gives

$$\mathbf{F}_{t/\tau_2}^{f_1*} = \mathbf{F}_{t/\tau_1}^f \cdot \mathbf{F}_0^{f*} \cdot (\mathbf{G}_{t/\tau_1}^{f_1})^{-1}, \quad (5)$$

and a similar expression can be found for fibers created at τ_2 . In general, therefore, the elastic deformation for fibers created at time τ is given as

$$\mathbf{F}_{t/\tau}^{f*} = \mathbf{F}_{t/\tau}^f \cdot \mathbf{F}_0^{f*} \cdot (\mathbf{G}_{t/\tau}^f)^{-1}. \quad (6)$$

In the current configuration $b(t)$, the volume fractions of the cells and fibers are ϕ^c and ϕ^f , respectively, with $\phi^c + \phi^f = 1$. The fiber volume fraction in the current configuration is given by

$$\phi^f(t) = \int_0^t \dot{\phi}^f(\tau) J_{\tau/t} d\tau, \quad (7)$$

where $\dot{\phi}^f(\tau)$ is the rate of fiber formation at time τ and $J_{\tau/t} = J_\tau J_t^{-1} = \det[\mathbf{F}_{\tau/0}^f \cdot (\mathbf{F}_{t/0}^f)^{-1}]$ accounts for the change in fiber volume from $b(\tau)$ to $b(t)$.

5.2. Stress and Equilibrium

The total Cauchy stress tensor is given as (Humphrey and Rajagopal, 2002)

$$\boldsymbol{\sigma}(t) = \phi^c(t) \boldsymbol{\sigma}^c(\mathbf{F}_t^{c*}) + \int_0^t \dot{\phi}^f(\tau) \boldsymbol{\sigma}^f(\mathbf{F}_{t/\tau}^{f*}) J_{\tau/t} d\tau, \quad (8)$$

where \mathbf{F}_t^{c*} and $\mathbf{F}_{t/\tau}^{f*}$ are given by Eqs. (3) and (6). We assume that the cells and fibers are nearly incompressible and only change shape as they contract, so that $J_{\tau/t} \cong 1$.

With inertial effects being negligible, morphogenesis can be treated as quasi-static, and the equilibrium equation is (Humphrey and Rajagopal, 2002)

$$\nabla \cdot \boldsymbol{\sigma} = 0, \quad (9)$$

where ∇ is the gradient operator defined in $b(t)$.

5.3. Constitutive Relations

Because of their high water content, soft biological tissues often are treated as incompressible materials. Not only does this assumption often lead to numerical challenges, but it really is not accurate. During deformation, water can enter or leave the tissue, as well as shift from one location to another within the tissue. For these reasons, we assume here that the blastoderm is *nearly* incompressible. In addition, to a first approximation, we assume that it is pseudo-elastic (Fung, 1993).

For a compressible pseudo-elastic material, the constitutive relation can be written in the form (Taber, 2004)

$$\boldsymbol{\sigma}^i = \frac{2}{J^{i*}} \mathbf{F}^{i*} \cdot \frac{\partial W^i}{\partial \mathbf{C}^{i*}} \cdot (\mathbf{F}^{i*})^T. \quad (10)$$

Here, $W^i(\mathbf{C}^{i*})$ is the strain-energy density function for cells ($i = c$) or fibers ($i = f$), $\mathbf{C}^{i*} = (\mathbf{F}^{i*})^T \cdot \mathbf{F}^{i*}$ is the right Cauchy-Green deformation tensor relative to the current zero-stress state,

and $J^{i*} = \det \mathbf{F}^{i*} \cong 1$ is the volume ratio (Taber, 2004). In the following, we drop subscripts on \mathbf{F} and related quantities with the understanding that \mathbf{F}^{c*} depends on t while \mathbf{F}^{f*} depends on t and τ .

Available experimental data suggest that tissues in the early embryo are relatively linear and isotropic (Xu et al., 2010; Zamir and Taber, 2004b), especially compared to mature tissues which have a more organized microstructure. Hence, the cells in the blastoderm are assumed to comprise a compressible isotropic material whose strain-energy density function is

$$W^c = \frac{\mu_c}{2} \left[I_1^* - 3 + \frac{1 - 2\nu}{\nu} \left((I_3^*)^{\frac{\nu}{1-2\nu}} - 1 \right) \right], \quad (11)$$

which is the form for a Blatz-Ko material (Taber, 2004), where the invariants are defined as $I_1^* = \text{tr} \mathbf{C}^{c*}$ and $I_3^* = (J^{c*})^2$. In addition, μ_c and ν are the shear modulus and Poisson's ratio, respectively, in the limit of small strain.

The fibers in the thin ring are modeled as a distinct transversely isotropic material. By construction, such fibers lie parallel to the wound margin, and the elastic stretch ratio of the fibers is given by

$$\lambda^{f*} = \sqrt{\mathbf{e}_\Theta \cdot \mathbf{C}^{f*} \cdot \mathbf{e}_\Theta}, \quad (12)$$

where \mathbf{e}_Θ is a unit vector parallel to the wound edge. Analogously, \mathbf{e}_R is a unit vector perpendicular to the wound edge, and \mathbf{e}_Z is normal to the plane of the membrane (see Appendix A), all in the undeformed (B_0) configuration. The corresponding unit vectors (\mathbf{e}_r , \mathbf{e}_θ , \mathbf{e}_z) in the current configuration $b(t)$ are given by (Taber, 2004)

$$\mathbf{e}_i = \frac{\mathbf{F} \cdot \mathbf{e}_I}{|\mathbf{F} \cdot \mathbf{e}_I|}. \quad (13)$$

For convenience, we refer to the R and Θ directions as radial and circumferential, respectively, even for elliptical wounds. Similarly, we refer to elliptical semiaxes as major and minor radii.

Each fiber is taken as an incompressible neo-Hookean bar with (Taber, 2004)

$$W^f = \frac{\mu_f}{2} \left[(\lambda^{f*})^2 + 2(\lambda^{f*})^{-1} - 3 \right]. \quad (14)$$

The fiber stress is given by Eq. (10) with

$$\mathbf{F}^{f*} = \lambda^{f*} \mathbf{e}_\theta \mathbf{e}_\theta + \lambda^{T*} (\mathbf{e}_r \mathbf{e}_r + \mathbf{e}_z \mathbf{e}_z) \quad (15)$$

where the transverse fiber elastic stretch ratio $\lambda^{T*} = 1/\sqrt{\lambda^{f*}}$ satisfies the incompressibility condition $\det \mathbf{F}^{f*} = 1$.

5.4. Single-Fiber Approximation

Equation (8) is a hereditary integral which depends on the histories of deformation and fiber deposition. As such, it introduces significant computational cost and complexity, and the time required to perform each simulation would make it impractical to find parameter values iteratively. To simplify the calculation, we take advantage of the separation in time scales of the healing mechanisms. The first phase of wound healing, driven by cellular contraction, is essentially complete by the time fibers form in significant quantity, while actin staining suggests that the bulk of the thin

ring forms within the first few minutes after wounding (Fig. 4). Hence, cell contraction is essentially constant as fibers form at a rate which is relatively fast compared to subsequent contraction and healing. As a first approximation, therefore, we take the reference configuration for all fibers in the thin ring to be the same, and set $\tau = 0$. Hence, we assume that the fibers accumulate relatively rapidly over the first few minutes of the healing process, while subsequent contraction takes place over a longer time scale. Then, Eq. (6) becomes

$$\mathbf{F}_{t/\tau}^{f*} \cong \mathbf{F}_{t/0}^{f*} = \mathbf{F}^{f*}(t) = \mathbf{F}_{t/0}^f \cdot \mathbf{F}_0^{f*} \cdot \left(\mathbf{G}_{t/0}^f\right)^{-1}. \quad (16)$$

With \mathbf{F}^{f*} no longer dependent on τ , Eq. (8) reduces to

$$\begin{aligned} \boldsymbol{\sigma}(t) &= \phi^c(t) \boldsymbol{\sigma}^c(\mathbf{F}^{c*}) + \boldsymbol{\sigma}^f(\mathbf{F}^{f*}) \int_0^t \dot{\phi}^f(\tau) d\tau \\ &= \phi^c \boldsymbol{\sigma}^c + \phi^f \boldsymbol{\sigma}^f, \end{aligned} \quad (17)$$

in which subscripts denoting time intervals have been dropped. In this approximation, the total deformation gradient tensor for a constrained mixture is given by $\mathbf{F} = \mathbf{F}^c = \mathbf{F}^f$, and Eqs. (2) and (16) yield

$$\mathbf{F} = \mathbf{F}^{c*} \cdot \mathbf{G}^c = \mathbf{F}^{f*} \cdot \mathbf{G}^f \cdot \left(\mathbf{F}_0^{f*}\right)^{-1}. \quad (18)$$

This equation gives the elastic deformation gradient tensors $\mathbf{F}^{c*} = \mathbf{F} \cdot (\mathbf{G}^c)^{-1}$ and $\mathbf{F}^{f*} = \mathbf{F} \cdot \mathbf{F}_0^{f*} \cdot (\mathbf{G}^f)^{-1}$, which are used in Eq. (10). With $\mathbf{G}^c(t)$, $\mathbf{G}^f(t)$, and \mathbf{F}_0^{f*} specified, we employ the single fiber approximation in the model described in the remainder of this section. In Appendix B we show that this approximation is sufficiently accurate for our purposes.

5.5. Contraction Dynamics

The cell contraction tensor \mathbf{G}^c is taken in the form

$$\mathbf{G}^c = G_R^c \mathbf{e}_R \mathbf{e}_R + G_\Theta^c \mathbf{e}_\Theta \mathbf{e}_\Theta + G_Z^c \mathbf{e}_Z \mathbf{e}_Z. \quad (19)$$

Since a cell contracts with little change in volume, we take $\det \mathbf{G}^c = G_R^c G_\Theta^c G_Z^c = 1$. Here, we consider three contraction schemes which define G_R^c , G_Θ^c , and G_Z^c in terms of a single specified cell contraction “stretch ratio” G^c :

$$G_R^c, G_\Theta^c, G_Z^c = \begin{cases} G^c, G^c, \frac{1}{(G^c)^2} & \text{isotropic contraction (} R, \Theta \text{ directions)} \\ 1, G^c, \frac{1}{G^c} & \text{circumferential contraction (} \Theta \text{ direction)} \\ G^c, 1, \frac{1}{G^c} & \text{radial contraction (} R \text{ direction).} \end{cases} \quad (20)$$

We will consider behavior of all three of these schemes. As discussed below, G^c is a specified function of time. Other choices of $(G_R^c, G_\Theta^c, G_Z^c)$ for circumferential and radial contraction schemes that preserve $\det \mathbf{G} = 1$, including those where $G_Z^c = 1$, do not significantly alter the behavior of the model (not shown).

Since \mathbf{G}^c is isochoric and the cells nearly incompressible, contraction causes cells to thicken in the Z direction, affecting cell stiffness (which is proportional to thickness). Because the epithelial membrane is restricted to lie in the plane, such thickening is the only deformation in the Z direction, and no out-of-plane bending is permitted.

To investigate whether rapid cell contraction in the thick ring drives the first phase of wound closure, we vary the degree of cell contraction G^c with both position and time. Outside of the thick ring, we set $G^c = 1$ at all times, indicating passive cells. Within the ring, G^c decreases with time from an initial value of 1 to the final value G_1^c . To avoid discontinuities, which can lead to numerical instabilities, the behavior of G^c transitions gradually at the ring boundary. We take G^c in the form

$$G^c(t, \rho) = 1 - [1 - g^c(t)] f^c(\rho), \quad (21a)$$

where f^c and g^c , respectively, govern the spatial and temporal aspects of G^c :

$$f^c(\rho) = \left[1 + \exp\left(\frac{\rho - \rho_c}{k_c}\right) \right]^{-1} \quad (21b)$$

$$g^c(t) = (1 - G_1^c) \exp(-t/\tau_c) + G_1^c. \quad (21c)$$

Here, τ_c is the characteristic cell contraction time (within the thick ring), ρ_c is the width of the thick ring, and k_c determines the width of the transition at the ring boundary. The distance from the wound edge ρ is given in Appendix A by Eqs. (A.3) and (A.6) for circular and elliptical wounds, respectively. Figure 7a shows $G^c(\rho)$ for various times.

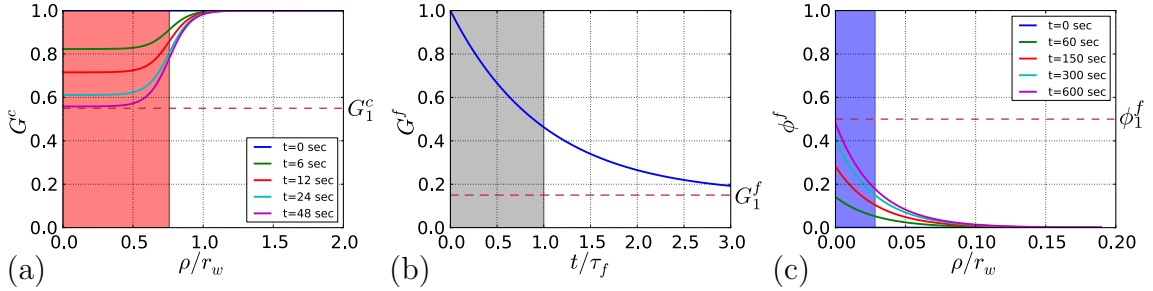


Figure 7: Cell and fiber contraction patterns, as well as fiber volume fraction, in the vicinity of the wound in the undeformed configuration. Parameters are given in Tables 2 and 3. (a) Cell contraction G^c (Eq. 21a) as a function of distance from wound edge ρ for various times, with ρ (see Appendix A) normalized by initial circular wound radius r_w . Shaded region indicates domain of thick cell ring. (b) Fiber contraction G^f (Eq. 23) as a function of time, normalized by τ_f . At the end of the simulation (600 sec, indicated by shaded region) G^f has decreased from 1 to 0.46. (c) Fiber volume fraction ϕ^f near the wound for various times (Eq. 24). Shaded region indicates nominal domain of fiber ring. Note that G^f is spatially uniform, with the extent of fiber ring given by ϕ^f .

Consistent with the single fiber approximation, the thin contractile ring forms with a prestretch F_0^{f*} and subsequently contracts (G^f decreases) while additional assembly occurs (ϕ^f increases). Fibers are assumed to contract only along their lengths, and the fiber prestretch and contraction tensors, respectively, are taken as

$$\mathbf{F}_0^{f*} = 1/\sqrt{F_0^{f*}} \mathbf{e}_r \mathbf{e}_R + F_0^{f*} \mathbf{e}_\theta \mathbf{e}_\Theta + 1/\sqrt{F_0^{f*}} \mathbf{e}_z \mathbf{e}_Z \quad (22a)$$

$$\mathbf{G}^f = 1/\sqrt{G^f} \mathbf{e}_R \mathbf{e}_R + G^f \mathbf{e}_\Theta \mathbf{e}_\Theta + 1/\sqrt{G^f} \mathbf{e}_Z \mathbf{e}_Z, \quad (22b)$$

which satisfies $\det \mathbf{F}_0^{f*} = \det \mathbf{G}^f = 1$, and both are symmetric relative to the cross-fiber direction. To define the dynamics of the fiber contraction ratio $G^f(t)$, we assume that G^f decreases expo-

nentially with time from $G^f = 1$ at $t = 0$ to a final value G_1^f at $t = \infty$, with the rate of decrease given by the characteristic time constant τ_f (Fig. 7b):

$$G^f(t) = (1 - G_1^f) \exp(-t/\tau_f) + G_1^f. \quad (23)$$

The spatial distribution of the thin ring is defined through ϕ^f , which varies both spatially and temporally. The value of ϕ^f is uniformly zero at $t = 0$, increases with time in the vicinity of the wound at a rate characterized by τ_ϕ , and approaches asymptotically the maximum value ϕ_1^f at the wound edge. After wounding ($t > 0$), the spatial distribution of ϕ^f takes the form of a decaying exponential away from the wound edge whose characteristic width ρ_f corresponds to the nominal thin ring width. Mathematically,

$$\phi^f(t, \rho) = \phi_1^f [1 - \exp(-t/\tau_\phi)] \exp(-\rho/\rho_f) \quad (24)$$

which is plotted in Fig. 7c.

5.6. Solution Procedure

All model simulations were performed using COMSOL Multiphysics (v 3.5a; Comsol, Inc.), with plane stress conditions assumed; see Taber (2008) as well as Appendix S.2 for more details about the implementation of growth. To establish initial conditions which correspond to the reference configuration b_0 at $t = 0$, the boundary stress is increased from zero in the undeformed configuration B_0 to the prescribed value σ_B , where it is subsequently held fixed for the remainder of the simulation. Because of the symmetry of the system, we simulate one quadrant of the epithelial membrane. We approximate an incision wound by an ellipse with a large AR, and use a triangular mesh of third-order Lagrange elements with a progressively finer mesh in the thick and thin ring regions, resulting in 4474 and 4419 elements in the circular and elliptical models, respectively. We perform a quasi-static analysis, with the direct UMFPAK spatial solver and BDM time stepper. Relative and absolute tolerances are 0.001, 0.0001, respectively. We found that the model converges successfully for the time period of interest (first 10 minutes) and that the results are not significantly different with the use of a finer mesh size. Furthermore, we found no evidence of numerical instabilities (e.g., extremely large stresses, deformations, or “checkerboarding”). Figure 5c illustrates the mesh geometry and boundary conditions of the finite-element model.

5.7. Parameter Values

The model parameters can be divided into three groups. Parameters defining the geometry of representative circular and elliptical wounds were obtained from our experimental data. A second set of parameters were obtained from experiments or deduced, and are considered known. A final set of parameters was determined by iteratively fitting the circular wound model to experimental results. These parameters were then used also for the elliptical wound model. In this section, we discuss the choice of the first two types of parameters, which are then considered “fixed.” The selection of the third type, considered “free” parameters, is discussed later.

5.7.1. Geometric Parameters

In constructing the model geometry we distinguish between the stress-free undeformed configuration B_0 and the reference configuration b_0 , which is deformed by the boundary stress σ_B but not

fiber or cell contraction (Fig. 5b). The geometry of the model is defined in the B_0 configuration, but is chosen such that dimensions in b_0 match experimental measurements.

Geometric Parameters	B_0	b_0
Circular wound radius	38 μm (R_w)	54 μm (r_w)
Elliptical wound major radius	82 μm (R_a)	91 μm
Elliptical wound minor radius	5.4 μm (R_b)	34 μm
Thick (cell) ring width	41 μm (ρ_c)	40 μm
Thin (fiber) ring width	1.5 μm (ρ_f)	1.3 μm
Membrane dimension	1020 μm	1140 μm

Table 2: Wound geometries for the model in undeformed (B_0) and reference (b_0) configurations (see Fig. 5). Membrane dimension is the length of the square epithelial membrane quadrant (Fig. 5c).

The circular wound radius r_w in b_0 was obtained from measurements immediately after wounding (see Section 4.1). The elliptical wound dimensions were chosen such that in b_0 the elliptical and circular wound areas are approximately equal, and the AR (=2.67) is consistent with experiment (Section 4.2). We approximate linear incisions with an elliptical wound of a relatively large aspect ratio (AR=15) for numerical reasons, since sharp corners introduce stress concentrations and lead to numerical instabilities (see also Appendix S.5). Thick and thin ring widths (ρ_c , ρ_f) were estimated from fluorescence microscopy images of circular wounds (Fig. 4), and k_c is taken as $\rho_c/10$. The same parameters are used for elliptical wounds.

A circular hole in a plate under tension perturbs the state of stress only locally, and its effect decays quickly with distance from the hole. At a distance of four wound diameters, the stress differs from the far field value by just 6% according to linear plate theory (Timoshenko and Goodier, 1951). Stress in our membrane model, although subject to relatively large deformations, is in generally good agreement with these theoretical predictions, and we choose the dimensions of the membrane to be at least an order of magnitude greater than the wound to eliminate far-field boundary effects. For computational efficiency we simulate a quarter of the entire domain, as illustrated in Fig. 5c.

Table 2 summarizes the geometric parameters, and Appendix A provides details of ring geometry specification.

5.7.2. Other Fixed Parameters

As discussed in Appendix C, we estimate the cell shear modulus to be $\mu_c \simeq 40$ Pa. Literature suggests a wide range of fiber stiffness values, from ~ 10 kPa (Lu et al., 2008) to well over 1 MPa (Deguchi et al., 2006), with fibers much stiffer than cells ($\mu_f \gg \mu_c$) (Rauzi and Lenne, 2011). We find that model sensitivity to μ_f decreases for $\mu_f \gtrsim 100 \mu_c$ as fiber dynamics alone dominate wound closure (data not shown), and thus choose $\mu_f = 80 \mu_c = 3.2$ kPa. We further chose ϕ_f to have a maximum value of 0.5, and note that model behavior depends on the product $\phi_f \mu_f$ (analysis not shown.)

The boundary tensile stress σ_B was estimated from previous work (Varner and Taber, 2010; Varner et al., 2010). Immediately after wounding, circular epithelial wounds open to a diameter approximately 1.2 times that of the punch used to make them (Varner et al., 2010), a result that corresponds to an equibiaxial membrane stretch ratio of 1.1 (Varner and Taber, 2010). We find that a boundary stress $\sigma_B = 1.05 \times \mu_c = 42$ Pa reproduces this strain. Model results are relatively insensitive to Poisson's ratio in the range $0.4 \leq \nu \leq 0.49$, and we take $\nu = 0.45$. Note that nearly incompressible models for anisotropic materials can be susceptible to errors for $\nu \rightarrow 0.5$ (Ní Annaidh

Material Parameters		
Fixed		
Cell shear modulus	μ_c	40 Pa
Boundary stress	σ_B	42 Pa
Poisson's ratio	ν	0.45
Final fiber fraction	ϕ_1^f	0.5
Fiber shear modulus	μ_f	3200 Pa
Free		
Cell contraction time	τ_c	12 sec
Fiber contraction time	τ_f	600 sec
Fiber formation time	τ_ϕ	180 sec
Cell final G	G_1^c	0.55
Fiber prestretch	F_0^{f*}	1.65
Fiber final G	G_1^f	0.15

Table 3: Cell and fiber parameters. Fixed parameters have values assumed to be known and were obtained as discussed in Section 5.7. Free parameter values were found by an iterative procedure so that circular wound model area trends reproduce those obtained by experiment (Section 6.2).

et al., 2013). All parameters used in the cell and fiber model, including those obtained from a fit to experiment (see below) are listed in Table 3.

6. Model Results

We now determine the remaining free parameters and examine whether the model captures the main features of the measured wound healing response.

6.1. Cellular Contraction is Relatively Isotropic in Thick Ring

Fluorescence microscopy images (Section 4.3) suggest that contraction at cell borders occurs within a thick ring around the wound, but do not indicate its nature. For example, is the contraction circumferential around the wound (like the contraction of an actomyosin cable) or isotropic? Other types of contraction anisotropy also may occur (Fig. 8a). Models of circular wounds are unable to discriminate between these possibilities, since multiple schemes can close a wound. Elliptical wound models, however, predict distinct temporal trends in the AR as the wound closes, and allow for competing contraction schemes to be critically evaluated.

Consider the area and AR of an elliptical wound for three different cell contraction schemes: isotropic, circumferential, and radial (see Eq. (20) and Fig. 8). As expected, radial contraction causes the wound to open further, allowing that scheme to be rejected. Both isotropic and circumferential contraction close the wound, but the AR trends differ qualitatively. For the circumferential case, the AR increases without bound, with the wound becoming increasingly slit-like as it heals. This behavior is at odds with experimental observations (Fig. 3). Isotropic contraction, by contrast, yields an AR that stays relatively constant as the wound closes, behavior generally consistent with experiment (Fig. 3).

We conclude, therefore, that cellular contraction in the thick ring is relatively isotropic, with cells on average contracting in both the radial and circumferential directions simultaneously. Future data may indicate that the contraction is actually anisotropic, but here we take contraction in the thick ring as isotropic to a first approximation. This scheme will be used for the thick ring in all subsequent models.

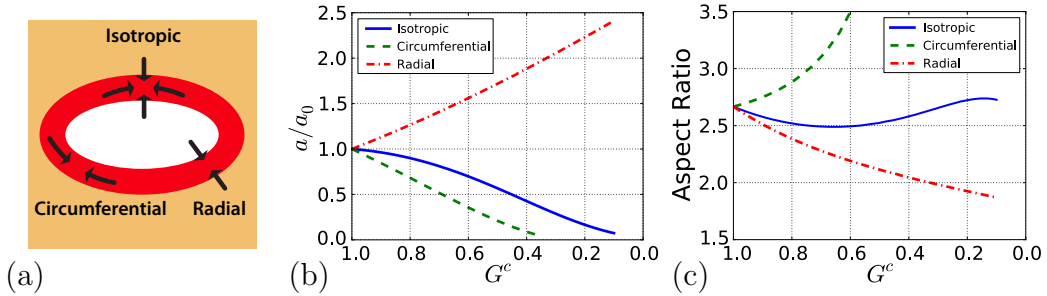


Figure 8: Area and aspect ratio (AR) trends for various cell contraction schemes for elliptical wound model. No fibers are present in these simulations (fiber fraction $\phi^f = 0$) and cell contraction G^c (Eq. 20) in the ring is specified directly (note, in model $G^c < G_1^c = 0.55$). Wound area a is normalized by area a_0 at $t = 0$. (a) The epithelial membrane in the cell ring can contract in both directions (isotropic) or in one direction only (radial or circumferential). (b, c) While the wound closes for both isotropic and circumferential schemes, only the isotropic case yields AR trends consistent with experiment. These trends are independent of σ_B .

6.2. Model-Predicted Changes in Wound Geometry Agree with Experimental Results

With the geometric and material parameters established in Section 5.7, six free model parameters remain: three that quantify the degree of contraction (F_0^{f*} , G_1^c , G_1^f) and three that characterize rates (τ_c , τ_ϕ , τ_f) (see Table 3). The goal is to find a set of biologically plausible parameter values that reproduce the average experimental circular wound area trends, i.e., the area given by Eq. (1). Multiple circular wound simulations were performed with systematically varying parameter values, which were adjusted iteratively to obtain an area vs. time curve that reasonably matches experiment.

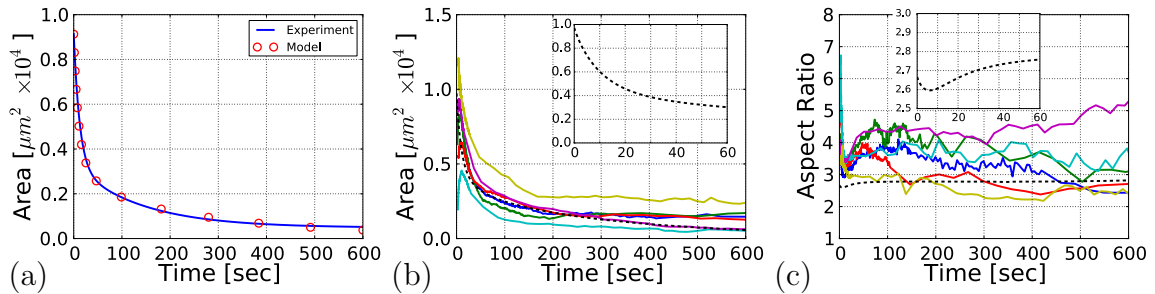


Figure 9: Comparison of experimental and model wound healing behavior. (a) Circular wound. Solid curve is the experimental wound area given by Eq. (1) with mean parameters from Table S1. Circles indicate model results (parameters from Table 3). (b,c) Elliptical wound. Solid curves show experimental area (b) and AR (c). Model results (dashed curve) use same parameters as circular wound. Insets detail model behavior in first minute, with same axis labels as main plot.

The healing response during the first 20-30 seconds is dominated primarily by cell contraction, as the fibers have not yet formed in significant quantity. The wound behavior during this time is controlled by the rate of cell contraction τ_c and the final cell contraction parameter G_1^c (see Eq. 21c). The values $G_1^c = 0.55$ and $\tau_c = 12$ sec reproduce this initial stage of contraction (Fig. 9a).

The parameters corresponding to the fiber prestretch (F_0^{f*}) and contraction (G_1^f) govern the remainder of wound closure. We find that fibers forming rapidly ($\tau_\phi = 180$ sec) in a state of

significant prestretch ($F_0^{f*} = 1.65$) and thereafter contracting more slowly ($\tau_f = 600$ sec, $G_1^f = 0.15$), together with the other parameters in Table 3, reproduce the experimentally observed area versus time curves quite well (Figure 9a). The uniqueness and biological plausibility of these values are discussed later.

Once obtained for circular wounds, these same parameters were then used in the elliptical wound model, with the resulting area and AR plotted in Figures 9b, c. From an experimental perspective, elliptical wounds are less reproducible, and we restrict ourselves to a qualitative comparison of wound trends. As in the case of circular wounds, and consistent with experimental trends, the elliptical wounds in the model close in two phases – a rapid initial closing followed by slower healing (Fig. 9b). The AR displays a brief decrease followed by a rebound and relatively constant value (Fig. 9c). Both features are broadly consistent with our experimental observations.

6.3. Peak Stresses Increase as Wounds Close

Stress distributions near the wound boundary are shown for circular wounds, with radial (σ_r) and circumferential (σ_θ) stress components plotted for four illustrative time points (Fig. 10). At $t = 0$ (i.e., b_0 configuration), the membrane is stretched passively by σ_B . Significant cell contraction has occurred by $t = 12$ sec, but fiber formation is negligible. At $t = 300$ and 600 sec, cell contraction is fully developed, with changes in stress driven by ongoing fiber formation and contraction.

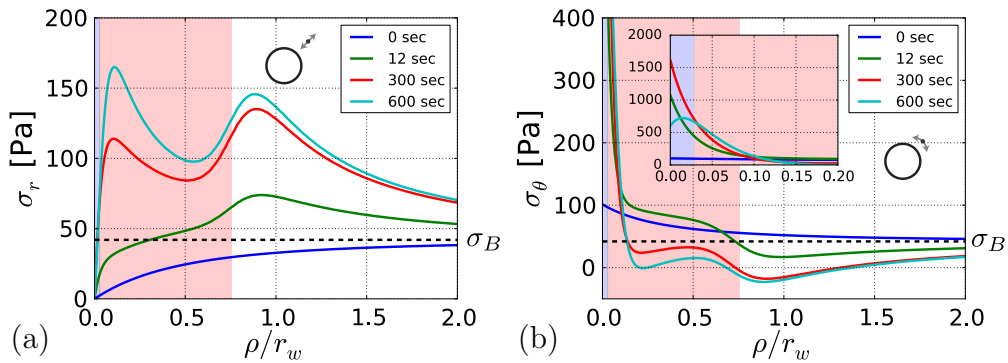


Figure 10: Epithelial membrane stress in the vicinity of circular wound. Icon indicates stress component (radial σ_r , circumferential σ_θ). Distance from wound edge in the reference configuration is given in multiples of the circular wound radius r_w , and the fiber and cell regions are indicated with blue and red shading, respectively (see Fig. 7). Inset in (b) details stress near wound boundary, with axes labels as in main figure. Far from the wound, both stress components approach the far-field value $\sigma_B = 42$ Pa.

For a circular wound, σ_r develops two peaks as the wound closes (Fig. 10a). One peak occurs near the wound edge, while the other develops just outside the thick ring. The distribution of σ_θ is dominated by a strong peak at the edge of the wound, increasing from about $2\sigma_B$ at $t = 0$ to $40\sigma_B$ at $t = 300$ sec. Thereafter σ_θ decreases at the wound edge and becomes slightly compressive immediately outside the cell ring; the reason for this effect is discussed later. In all cases, both stresses approach the far-field value σ_B away from the wound.

Stress distributions near an elliptical wound exhibit similar characteristics (Fig. S4). For an ellipse, the strongest stress concentrations occur near the wound edge along the major axis, while the stresses are reduced relative to those for a circular wound along the minor axis.

6.4. Elliptical Wounds Briefly Open at Low Tension

The principal effect of varying σ_B is to change the initial size of the wound. Also, as σ_B increases, elliptical wounds become initially rounder (Fig. 11a).

For a circular wound, area decreases in a similar manner regardless of σ_B , with wounds under higher tension closing more rapidly (Fig. 11b). Elliptical wounds at high tension likewise begin to close immediately after contraction begins, but for $\sigma_B \lesssim 15$ Pa the wound area increases momentarily before closing (Fig. 11b). This initial ‘‘gaping’’ of elliptical wounds at low σ_B is associated with a rapid decrease in the wound AR (Fig. 11c). Similar behavior was observed experimentally, where some elliptical wounds initially increased in area while becoming more round (Fig. 3), but it is important to note tissue tension σ_B was not determined experimentally.

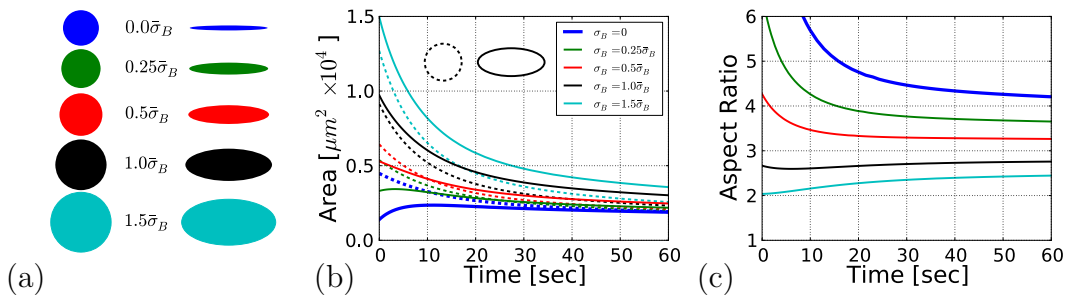


Figure 11: Effect of tension σ_B on circular and elliptical model wounds. (a) Wound size and shape at $t = 0$ (a_0) for different σ_B . Tension is relative to $\bar{\sigma}_B = 42$ Pa (Table 3). (b) Area for circular wounds (dashed curves) and elliptical wounds (solid curves) with different constant values of σ_B . (c) Aspect ratio (AR) for elliptical wounds. Low initial tension in elliptical wounds results in a brief increase in wound area and a sharp decrease in AR.

This transient area increase is driven primarily by a brief expansion of the minor radius of the wound (Fig. S9a). This effect is captured by the elliptical wound model when the initial tension is reduced. With σ_B set to the estimated physiological value $\sigma_B = 42$ Pa (Table 3), the area decreases immediately after wounding (Fig. 11b,c) and both the major and minor axes decrease (Fig. S9b), with the AR remaining relatively constant (Fig. 11c). For low σ_B wound area increases, the minor axis increases, and the AR decreases briefly just after contraction begins (Fig. 11b,c, S9b). The reason behind this behavior is discussed later. The qualitative aspects of wound closure are relatively insensitive to wound size and shape (see Supplemental Appendix S.5).

7. Discussion

Our results suggest that wounds in the early chick embryo heal by three distinct and essentially sequential mechanisms. First, during about the first 30 seconds, a ring of cells (3-4 cells deep) contracts to quickly close the wound area by more than 50%. Second, a relatively thin contractile ring forms at the wound edge and contracts more slowly to close the wound nearly completely over a period of several minutes. Finally, filopodia pull and zip the edges of the wound together to complete the healing process. The last two phases have been known for some time (Jacinto et al., 2001; Woolley and Martin, 2000), and the initial rapid healing phase was observed in chick embryos by Bortier et al. (1993), but they did not investigate it in detail. Notably, this phase seems to be absent in *Drosophila* embryonic wounds (Abreu-Blanco et al., 2011; Hutson et al., 2009; Ma et al., 2009), so it may not be a universal phenomenon.

As discussed below, our model captures the fundamental behavior of the first two phases of wound healing and yields insight into the detailed mechanics. Because it does not include filopodial zippering, however, the utility of our model is restricted to wounds relatively large compared to cell size. At time scales on the order of hours the assumption that the blastoderm can be treated as a single-layered membrane also breaks down, as germ layers develop and move with respect to one another. As a result, our model is valid from the first few seconds to ten minutes or so after wounding.

7.1. Parameter Values for Contraction Dynamics

For our wound healing model to be plausible, it is important that the values of the free parameters are consistent with those reported in the literature for related systems. Our model incorporates three separate time constants (Table 3): τ_c for cell contraction, τ_ϕ for fiber formation, and τ_f for fiber contraction. Three additional parameters specify the degree of initial and final contraction: final cell contraction is given by G_1^c , and initial (prestretch) and final fiber contractions are given by $(F_0^{f*})^{-1}$ and G_1^f , respectively.

The rate of cell contraction τ_c (12 sec) matches the time constant T_1 (12.4 sec) for the first phase of healing circular wounds (Section 4.1, Table S1). Both the speed and magnitude of cell contraction ($G_1^c = 0.55$) are in line with observations for smooth muscle cells (An and Fredberg, 2007). The rate of fiber formation τ_ϕ (3 min) is consistent with our observed time rate of fiber formation (see Fig. 4 and Sec. 7.2.1), and the fiber contraction rate τ_f (20 min) is consistent with actomyosin fiber dynamics continuing over tens of minutes following a stimulus (An and Fredberg, 2007; Brock et al., 1996). Embryonic tissues can shorten by 70% or more within a relatively short time period (Varner and Taber, 2012b), supporting the value $G_1^f = 0.15$. Such a large contraction likely involves significant remodeling of actomyosin fibers, similar to that observed in smooth muscle cells (Matsumoto and Nagayama, 2012) or the contractile ratcheting mechanism described by Martin et al. (2009).

Finally, the dynamics of wound closure are quite sensitive to the value of the prestretch F_0^{f*} (Fig S12a). Our value ($F_0^{f*} = 1.65$) is somewhat larger than that reported in the literature (1.10 to 1.35; Kaunas and Deguchi 2011). This is discussed further in Section 7.2.2.

The parameters in Table 3 are not unique. For instance, a set of parameters where fibers form slowly ($\tau_f = 20$ min) with a larger prestretch $F_0^{f*} = 3.1$ and without further contraction ($G_1^f = 1$) can also reproduce our wound closing results (Fig. S12b). Our experimental data are insufficient to discriminate between these and other possible parameter sets, and this certainly warrants further study.

7.2. Phases of Embryonic Wound Healing

Unlike adult wounds, embryonic wounds generally heal quickly without leaving a scar (Redd et al., 2004). The healing process involves many of the same mechanisms used for morphogenesis (Wood et al., 2002), which often produce dramatic and rapid changes in tissue shape driven by contractile forces (Davies, 2005). Fusion of epithelia is also common, e.g., during neurulation and heart tube formation (Colas and Schoenwolf, 2001; Moreno-Rodriguez et al., 2006; Ray and Niswander, 2012). The three healing phases close wounds efficiently and robustly.

7.2.1. Phase 1: Rapid Cellular Contraction (Thick Ring)

Activation of upstream GTPase regulators of actin and myosin occurs 10-20 seconds after wounding (Bement et al., 2006; Clark et al., 2009), and wound-induced actomyosin structures are

first observed 1-3 minutes following wounding in a variety of organisms (Brock et al., 1996; Kasza and Zallen, 2011). These characteristics are consistent with our observations on the formation and contraction of the thin contractile ring (see Sec. 7.2.2 and Figs. 4b,e). However, we have found that healing actually begins within seconds of wounding, ruling out the possibility of *de novo* actomyosin assembly in the first phase.

Presumably, the initial rapid-healing phase is instead powered by pre-existing cellular cytoskeletal structures. Epithelial cells generally contain a ring of actin and myosin associated with adherens junctions around cell borders (Lodish et al., 2004) (Figs. 4a,d), and contraction of these fibers plays a role in many morphogenetic processes (Martin, 2010; Rauzi and Lenne, 2011). Shortening of these relatively randomly oriented fibers would result in tissue-level isotropic contraction, consistent with our model. A possible signal for the contractile response is calcium (Ca^{2+}), which can induce swift but short-lived actomyosin contraction (Cordeiro and Jacinto, 2013; Tomasek et al., 2002), is rapidly modulated (Clark et al., 2009; Xu and Chisholm, 2011), can be activated several cell layers away from the wound (Klepeis et al., 2001; Woolley and Martin, 2000; Xu and Chisholm, 2011), and has been implicated in a variety of wound healing processes (Benink and Bement, 2005; Sonnemann and Bement, 2011). Thus, the proposed cell contraction mechanism is reasonable from a cellular biological perspective.

Most previous studies of embryonic wound healing have focused on time scales of a minute or longer, but Bortier et al. (1993) mention in passing rapid dynamics of chick epithelial wounds similar to those we report here. The authors note that “the wounds showed a viscoelastic reaction upon wounding: they enlarged within one second, immediately followed by a narrowing, until wound diameters were between the original and largest size. After these reactions the wound submarginal region was thickened...” No further discussion or analysis of this healing mechanism is provided and, to our knowledge, other investigators have not addressed this observation. It seems likely that the submarginal region, reported as 75-150 μm wide, corresponds to the thick ring where isotropic contraction occurs. The authors also observed blebbing cells in this region, while cell bulging and “mounding”, as well as tissue thickening, has been reported near the margin of embryonic wounds in several organisms (England and Cowper, 1977; Jacinto et al., 2001; Smedley and Stanisstreet, 1984; Stanisstreet et al., 1980). Both cell bulging and blebbing suggest high intracellular pressure (Charras et al., 2008), which is consistent with strong isotropic contraction.

7.2.2. Phase 2: Slow Fiber Contraction (Thin Ring)

Following the creation of a multicellular wound, actin and myosin are recruited to the wound margin where they assemble a continuous supracellular cable which spans cells through adherens junctions. The cable forms over the course of minutes and contracts to generate tension which helps close the wound (Brock et al., 1996; Clark et al., 2009; Kiehart, 1999; Martin and Lewis, 1992; Sonnemann and Bement, 2011). Contractile actomyosin cables are used by the embryo in a variety of contexts, for example to divide cells and close the dorsal ectoderm in *Drosophila*, as well as to heal wounds (Davies, 2005; Rodriguez-Diaz et al., 2008; Sonnemann and Bement, 2011). Studies of actomyosin dynamics at high temporal and spatial resolution have shown contraction to be pulsatile, with periods of active shortening occurring between periods of quiescent stabilization (Gorfinkiel and Blanchard, 2011; Levayer and Lecuit, 2012; Martin, 2010). We did not observe such pulsatility, as localized pulses may be averaged out over the perimeter of a multicellular wound, and we did not include this in the model. Being relatively stiff, the fiber ring can generate the force needed to overcome the high circumferential stresses that develop as the wound closes (Fig. 10) (Stricker et al., 2010).

The remodeling theory used in our model was originally developed to describe the turnover of passive tissue constituents, e.g., elastin and collagen, which are thought to be created with significant prestretch (Humphrey and Rajagopal, 2002). It is not clear, however, that actomyosin fiber assembly involves an initial stretch. Hence, we interpret F_0^{f*} as the result of a rapid contraction of the initially unloaded fiber (time constant $\tau_{un} \ll \tau_f$) that slows ($\tau_{un} \rightarrow \tau_f$) as tension increases, with the observed prestretch $F_0^{f*} = (G^f)^{-1}$ resulting from the contribution of many such fibers. This Hill-like behavior is consistent with some recent models for stress fibers (Deshpande et al., 2007; Stachowiak and O’Shaughnessy, 2008), and an ability of actomyosin fibers to rapidly contract by large amounts has been observed in smooth muscle cells (An and Fredberg, 2007).

7.2.3. Phase 3: Filopodial Zippering

Filopodia-mediated zippering is also an important wound healing mechanism in early chick embryos. Although cell protrusions have not been reported during wound healing in older chick embryos (Brock et al., 1996; Martin and Lewis, 1992), filopodia, lamellipodia, and microvilli have been seen at early (HH 3-5) embryonic stages (England and Cowper, 1977; Mareel and Vakaet, 1977; Stanisstreet et al., 1980), and were apparent here as well (Fig. 4f, S1). Such protrusions can contact and pull cells at opposite sides of the wound together, closing it by a zippering mechanism (Jacinto et al., 2000; Wood et al., 2002). Because of their short length ($\sim 5 \mu\text{m}$ (Wood et al., 2002)), filopodia and related structures are unlikely to play a significant role until the wound opening is relatively small. Such effects are not captured by our model.

The three active processes – isotropic cell contraction, actomyosin ring contraction, and filopodial zippering – work together to close a wound, a redundancy which has been observed in other morphogenetic processes (Davidson et al., 2002; Jacinto et al., 2001; Kiehart et al., 2000). Very small wounds tend to close quickly (data not shown), with isotropic contraction likely playing the dominant role. The capacity of this mechanism is limited, however, and large wounds require a contractile ring. In some cases wounds never heal, or heal so slowly that closing does not occur during the period of observation. The reason may be that they are created in areas of older embryos where blastoderm tension is high (Varner et al., 2010), or they excessively perturb the tissue past the point of viability. Nevertheless, the capacity of the early chick embryo to heal is remarkable, and we find that nearly all wounds, if given enough time, do close.

7.3. Mechanics of Wound Closure

The way circumferential contraction closes a wound is consistent with physical intuition, i.e., by shortening the perimeter. The mechanics of embryonic wound healing, however, contain some subtleties that warrant discussion. In particular, geometric effects, coupled closely to mechanics, can lead to counter-intuitive behavior in the elliptical wound (e.g., gaping under low tension) which is not observed in circular wounds, even though the underlying contractile mechanisms and model parameters are the same.

For example, it is important to note that cellular contraction occurs with little or no change in cell volume. Hence, circumferential contraction is accompanied by radial expansion, which helps healing by pushing the edges of the wound inward. Because of structural stiffening in regions of high curvature, these radial stresses deform edges along the minor axis of elliptical wounds more easily than those along the major axis, causing the wound to become more slit-like. This explains in part why the AR increases for the case of circumferential contraction only (Fig. 8c). In contrast, radial contraction pulls the long edges outward, increasing the AR (Fig. 8c).

Since radial and circumferential contraction in the thick ring have opposite effects on the AR, these two effects essentially cancel out for isotropic contraction, and the wound shape remains relatively constant as it closes (Fig. 8c). The interaction of these effects with stress-induced elastic deformation underlies the initial opening of the elliptical wounds in membranes subjected to relatively small tension (Fig. 11b). As the applied tension increases, the stress concentrations near the edge of the wound increase. Since radial stress is considerably smaller than circumferential stress near the wound edge (Fig. S4), radial contraction is more effective initially than circumferential contraction, and the wound first opens before starting to close. Hence, the detailed wound geometry depends on a balance between radial and circumferential contraction, as well as the tissue stresses developed in these directions.

Another item of note is that inward radial movement of the membrane reduces its perimeter and tends to decrease circumferential stress. Unless this “slack” is taken up by circumferential contraction, compression can result. This effect is clearly seen in plots of σ_θ (Fig. 10), where the circumferential stress decreases, and in some cases becomes negative, immediately outside of the thick ring, as well as inside the ring toward the end of the simulation. In a physical system such compression, if large enough, would manifest as buckling or wrinkling of tissue. Careful observation with a stereomicroscope revealed no such out-of-plane folding or buckling.

The stress concentrations predicted by our model, particularly around elliptical wounds, are of a magnitude consistent with fiber stress exerted by smooth muscle cells (An and Fredberg, 2007). Viscoelastic effects, not incorporated in the model, are likely to reduce the peak stress considerably. Overall, the coupling between passive stretch, active contraction, and nonlinear geometric effects driven by large tissue deformation resist simple explanation and highlight the utility of computational models.

7.4. Conclusions and Future Work

The results of our study suggest that wound healing in embryonic epithelia consists of three main sequential phases: (1) rapid contraction of actomyosin fibers at cell borders within a relatively thick zone near the wound (approximately isotropic at the tissue scale); (2) slower contraction of a thin supracellular actomyosin ring at the wound margin; and (3) filopodia-mediated zippering of the wound edges. While the latter two phases have been studied in considerable detail (Wood et al., 2002), the first phase has apparently remained unknown or underappreciated by most previous investigators.

Several aspects of this problem warrant future investigation. For example, work is needed to determine the molecular mechanisms that regulate the formation and activity of the contractile fibers, as well as how this activity is integrated to produce tissue-level forces (see related work by Hutson et al. (2003)). Also, mechanical signals govern the spatiotemporal contractility of tissue in a variety of ways (Gorfinkiel and Blanchard, 2011; Hutson and Ma, 2008; Levayer and Lecuit, 2012; Vogel and Sheetz, 2006; Wozniak and Chen, 2009), and mechanical feedback has long been suggested to play a role in wound healing (Martin and Lewis, 1992). While we have recently proposed a mechanical feedback model for embryonic wound healing (Taber, 2009), this is not included in the current model.

Finally, it is important to note that other mechanisms may be involved in embryonic wound healing. Some of these may be redundant mechanisms that activate when contraction fails. For example, increased adhesion affinity between cells can cause them to elongate radially and shorten circumferentially, creating tension that helps close the wound. Cell rearrangement may also play

a role. Ultimately, a complete understanding of embryonic wound healing will require integrating experiments and computational models across multiple disciplines as well as multiple scales.

Appendix A. Contractile Ring Geometry

For clarity, in this appendix we use the notation (R, Θ, Z) for cylindrical polar and (ξ, η, Z) for elliptical cylindrical coordinates, respectively. In the body of the manuscript, for convenience we use (R, Θ, Z) to refer to coordinates in both coordinate systems, with the understanding that $\xi = R$ and $\eta = \Theta$ in the context of an elliptical geometry. Lower and upper cases refer to current (b) and undeformed (B_0) configurations, respectively.

Appendix A.1. Coordinate Systems

Because the contractile fibers are oriented parallel to the wound edge, we construct coordinate systems with a unit vector lying parallel to the fibers in the undeformed state B_0 . For circular wounds we use a cylindrical polar coordinate system, which relates the coordinates (R, Θ, Z) to the Cartesian (X, Y, Z) coordinates as (Fig. 12a)

$$X = R \cos \Theta, \quad Y = R \sin \Theta, \quad Z = Z \quad (\text{polar}). \quad (\text{A.1})$$

For an elliptical wound centered at the origin with foci at positions $\pm\alpha$ on the X axis, the coordinates (X, Y, Z) relate to the elliptical cylindrical coordinates (ξ, η, Z) as (Arfken and Weber, 2005) (Fig. 12b)

$$X = \alpha \cosh \xi \cos \eta, \quad Y = \alpha \sinh \xi \sin \eta, \quad Z = Z \quad (\text{elliptical}). \quad (\text{A.2})$$

The unit vectors \mathbf{e}_R and \mathbf{e}_ξ are normal to the wound edge in the polar and elliptical undeformed coordinate systems, respectively, while \mathbf{e}_Θ and \mathbf{e}_η are tangent to the wound edge. In both cases \mathbf{e}_Z is normal to the plane of the membrane.

Appendix A.2. Contractile Ring Width

To construct rings of uniform width around a wound in the undeformed state B_0 , we calculate the distance from any given point \mathbf{Q} to the wound edge. For a circular wound this task is straightforward. We define $\mathbf{R} = R_R \mathbf{e}_R$ as the nearest point on the wound edge to $\mathbf{Q} = R_Q \mathbf{e}_R$ (Fig. 12a). Thus, the magnitude of the vector $\boldsymbol{\rho} = \mathbf{Q} - \mathbf{R} = \rho \mathbf{e}_R$ is given simply as,

$$\rho = R_Q - R_R \quad (\text{polar}). \quad (\text{A.3})$$

An analogous approach fails in elliptical coordinates because the vector $(\xi_Q - \xi_R)\mathbf{e}_\xi$ does not have a uniform length around the perimeter of the wound (Fig. 12b). Instead, we define \mathbf{R} as the point on the wound edge with the same η coordinate as \mathbf{Q} , and expand \mathbf{Q} as a Taylor series in $d\xi = \xi_Q - \xi_R$ about \mathbf{R} . Retaining terms to $O(d\xi^2)$, we write

$$\begin{aligned} \boldsymbol{\rho} &= \mathbf{Q} - \mathbf{R}, \\ &\simeq \left(\mathbf{R} + \left. \frac{\partial \mathbf{R}}{\partial \xi} \right|_{\mathbf{R}} d\xi + \frac{1}{2} \left. \frac{\partial^2 \mathbf{R}}{\partial \xi^2} \right|_{\mathbf{R}} d\xi^2 \right) - \mathbf{R}, \\ &= \left. \frac{\partial \mathbf{R}}{\partial \xi} \right|_{\mathbf{R}} d\xi + \frac{1}{2} \left. \frac{\partial^2 \mathbf{R}}{\partial \xi^2} \right|_{\mathbf{R}} d\xi^2. \end{aligned} \quad (\text{A.4})$$

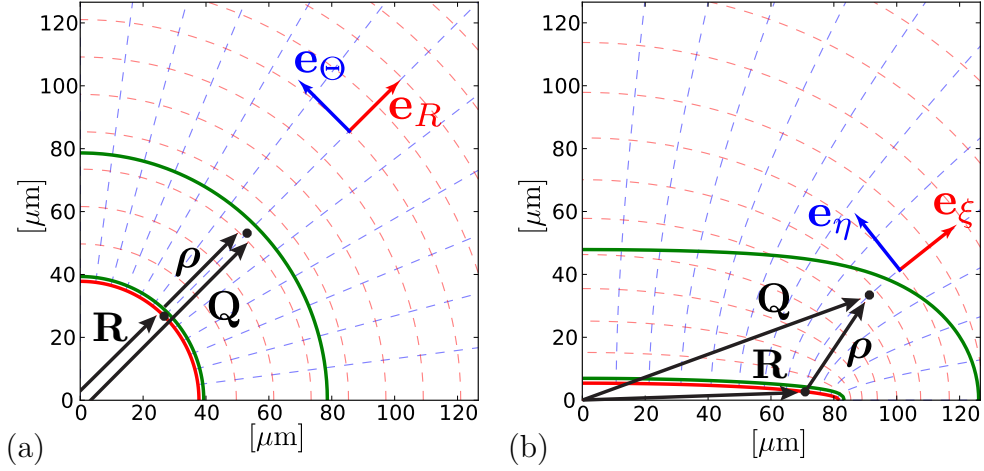


Figure 12: Detail of model geometry in the immediate vicinity of the wound in the undeformed (B_0) configuration for circular (a) and elliptical (b) wounds. Because of symmetry, only one quadrant of the membrane is considered, and the wound lies in the lower-left corner. The solid red curve indicates the wound boundaries, and the green curves mark the boundaries of the thin and thick rings. Dashed blue and red curves indicate direction along the circumferential (\mathbf{e}_Θ and \mathbf{e}_η) and radial (\mathbf{e}_R and \mathbf{e}_ξ) directions, respectively. The vector $\boldsymbol{\rho}$ marks the distance between an arbitrary vector \mathbf{Q} and a corresponding vector \mathbf{R} on the wound edge. In panel (a) these colinear vectors have been separated for clarity.

Using Eq. (A.2), we can write the derivatives of $\mathbf{R} = X \mathbf{e}_X + Y \mathbf{e}_Y$ as

$$\begin{aligned} \left. \frac{\partial \mathbf{R}}{\partial \xi} \right|_{\mathbf{R}} &= \alpha \sinh \xi_R \cos \eta_Q \mathbf{e}_X + \alpha \cosh \xi_R \sin \eta_Q \mathbf{e}_Y, \\ \left. \frac{\partial^2 \mathbf{R}}{\partial \xi^2} \right|_{\mathbf{R}} &= \alpha \cosh \xi_R \cos \eta_Q \mathbf{e}_X + \alpha \sinh \xi_R \sin \eta_Q \mathbf{e}_Y. \end{aligned} \quad (\text{A.5})$$

Finally, from Eq.(A.4) we find the magnitude of $\boldsymbol{\rho}$ for the elliptical wound as

$$\begin{aligned} \rho &= \frac{\alpha}{2} \left[(2 \sinh \xi_R d\xi + \cosh \xi_R d\xi^2)^2 \cos^2 \eta_Q + \right. \\ &\quad \left. (2 \cosh \xi_R d\xi + \sinh \xi_R d\xi^2)^2 \sin^2 \eta_Q \right]^{1/2} (\text{elliptical}), \end{aligned} \quad (\text{A.6})$$

where ξ_R is constant along the wound edge and η_Q is given by \mathbf{Q} . While this approximation strictly holds only for \mathbf{Q} in the immediate neighborhood of \mathbf{R} , it serves as an adequate approximation over the domain of both contractile regions.

Given the model geometry (Table 2), we find the focus position $\alpha = 82.8 \mu\text{m}$ and ξ at wound boundary $\xi_R = 0.0663$. The contours of ρ equal to ρ_f and ρ_c , which demarcate the borders of the fiber and cell contractile regions, respectively, are plotted in Fig. 12b, and we find that ρ in the elliptical coordinates evaluated along the X and Y axes in the B_0 configuration varies less than 5%.

Appendix B. Comparison of Single and Multiple Fiber Models

To evaluate the accuracy of the single-fiber approximation, we consider the simple case of an unstretched homogeneous bar fixed at both ends (Fig. 13 inset), and neglect the contribution of cells by setting $\mu_c = 0$. In this one-dimensional approximation, $F^{f*} = \lambda^{f*}$, $F_0^{f*} = \lambda_0^{f*}$, $C^{f*} = \lambda^{f*2}$, and $J^{f*} = 1$. For simplicity we set $\mu_f = 1$ and $\lambda_0^{f*} = 1$, and write the stress as a linear function of the elastic stretch ratio,

$$\sigma^f = \lambda^{f*} - 1. \quad (\text{B.1})$$

For the multiple-fiber model, the fiber stretch ratio is given by Eq. (6) as

$$\lambda_{t/\tau}^{f*} = \frac{\lambda_{t/\tau}^f}{G_{t/\tau}^f}, \quad (\text{B.2})$$

and for the single-fiber model, Eq. (18) gives

$$\lambda^{f*} = \frac{\lambda}{G^f}. \quad (\text{B.3})$$

In the present isometric problem, the total stretch ratios are $\lambda_{t/\tau}^f = \lambda = 1$.

With the above equations, the fiber stress, given by the 1-D forms of Eqs. (8) and (17), is

$$\sigma_{MF}(t) = \int_0^t \dot{\phi}^f(\tau) \left(\frac{1}{G_{t/\tau}^f} - 1 \right) d\tau \quad (\text{B.4})$$

for the multiple-fiber model and

$$\sigma_{SF}(t) = \phi^f(t) \left(\frac{1}{G^f} - 1 \right) \quad (\text{B.5})$$

for the single-fiber model.

For illustrative purposes, we take $G^f(t) = \exp(-t/\tau_f)$ for the single-fiber model. This gives

$$G_{t/\tau}^f = G^f(t)/G^f(\tau) = \exp[-(t - \tau)/\tau_f] \quad (\text{B.6})$$

for the multi-fiber model. The fiber fraction, from Eq. (24), is

$$\phi^f(t) = 1 - \exp(-t/\tau_\phi). \quad (\text{B.7})$$

We also nondimensionalize time by the fiber contraction rate and define

$$\begin{aligned} t' &\equiv t/\tau_f, \\ \alpha &\equiv \tau_f/\tau_\phi. \end{aligned} \quad (\text{B.8})$$

Finally, we can write Eqs. (B.4) and (B.5) as

$$\begin{aligned}\sigma_{MF}(t') &= \frac{1}{1+\alpha} \exp(-\alpha t') + \frac{\alpha}{1+\alpha} \exp(t') - 1 \\ \sigma_{SF}(t') &= [1 - \exp(-\alpha t')] [\exp(t') - 1]\end{aligned}\tag{B.9}$$

where the multi-fiber stress was integrated analytically. Both stresses are parameterized by α , which is large when fibers form quickly and contract slowly, and small when the opposite is true.

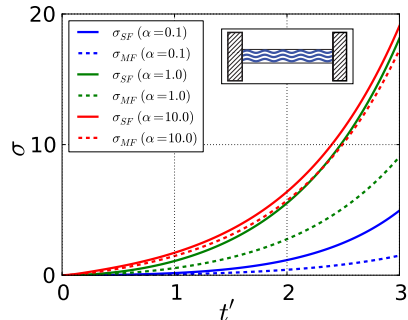


Figure 13: Fiber stress in a homogeneous bar with fixed ends (inset) as a function of non-dimensional time t' for different fiber models and values of α . In all cases $\sigma_{SF} \geq \sigma_{MF}$, but this difference decreases with large α .

The stresses σ_{MF} and σ_{SF} are plotted for a range of α (Fig. 13). Differences between the single and multi-fiber models decrease with increasing α . As $\alpha \rightarrow \infty$ all fibers appear instantaneously at $t = 0$, so that the two models yield identical results. The parameters used in the body of the manuscript correspond to $\alpha = 3.3$ (Table 3). We conclude that the single fiber model, while a simplification of a more biologically realistic multi-fiber formulation, is sufficiently accurate for the chosen parameters to justify its significant computational advantages.

Appendix C. Mechanical Properties of Blastoderm

To estimate the mechanical properties of the early chick blastoderm (i.e., a value for μ_c), we constructed a simple linear model for indentation of a plate under in-plane tension, and used it to simulate microindentation experiments of HH stage 5 embryos previously conducted in our laboratory (Zamir et al., 2003; Varner et al., 2010; Varner and Taber, 2012a). Briefly, following the framework employed by (Zamir and Taber, 2004a), we model the blastoderm near the indenter as a thin, isotropic annular plate under in-plane tension. For small deflection, the governing differential equation is given by (Szilard, 1974)

$$D_p \nabla^4 w - T_r \nabla^2 w = p,\tag{C.1}$$

where w is the transverse deflection, ∇ is the gradient operator, $D_p = Eh^3/12(1-\nu)^2$ is the flexural rigidity, T_r is the radial in-plane force per unit length, p is the applied surface pressure, E is the Young's modulus, ν is Poisson's ratio, and h is the plate thickness.

Here, we consider the case of a circular plate clamped at the outer radius b , which represents the distance at which the local disturbance from the indenter is effectively zero. The plate also is

taken as fixed at the inner radius to a rigid cylindrical indenter of radius a that exerts a force P . The boundary conditions take the form

$$\begin{aligned} V(a) &= -\frac{P}{2\pi a}, \\ \Theta(a) &= 0, \\ w(b) &= 0, \\ \Theta(b) &= 0, \end{aligned} \tag{C.2a}$$

where V is the transverse shear per unit length and Θ is the rotation. Note that, in this case, no surface pressure is applied to the plate (i.e., $p = 0$), so the applied load enters not through any specific term in equation (C.1), but rather through enforcement of the boundary condition (C.2).

Hole punching experiments in HH stage 5 embryos have indicated that the blastoderm is initially in an approximately uniform, equibiaxial state of tension (Varner and Taber, 2010; Varner et al., 2010). In addition, comparing the geometry of the wounds to the dimensions of the punching pipette have revealed that the initial tissue strains are $\epsilon_r = \epsilon_\theta \equiv \epsilon \simeq 0.1$. For plane stress, the tension is then given by

$$\begin{aligned} \sigma_r = \sigma_\theta &= \frac{E}{1 - \nu^2}(\epsilon + \nu\epsilon), \\ &= \frac{E\epsilon}{1 - \nu}. \end{aligned} \tag{C.3}$$

If we assume material incompressibility (i.e., $\nu = 0.5$) and $\epsilon = 0.1$, then

$$T_r = \sigma h = 0.2Eh. \tag{C.4}$$

Microindentation experiments performed in our laboratory have indicated an approximate blastodermal stiffness of 0.2-0.6 mdyne/ μm using an indenter with a radius $a = 10 \mu\text{m}$ (Varner et al., 2010; Varner and Taber, 2012a). Moreover, optical coherence tomography reconstructions of early chick embryos have shown the thickness of the blastoderm to be approximately $h = 50\text{--}90 \mu\text{m}$ (Varner et al., 2010).

If we use these values in combination with equation (C.4) and take the distance from the embryonic midline to the boundary of the area pellucida ($\sim 1\text{--}2 \text{ mm}$) as the radius of the circular plate b , we can solve equations (C.1) and (C.2) for different values of E and compare the computed stiffness values, given by $P/w(a)$, to those reported experimentally (Varner and Taber, 2012a). Doing so indicates an approximate Young's modulus of 120 Pa for the blastoderm, which (given material incompressibility) yields the shear modulus $\mu_c = E/3 = 40 \text{ Pa}$.

Acknowledgments

This work was supported by grants F32 GM093396 (MAW), R01 GM075200 and R01 N5070918 (LAT) from the National Institutes of Health, as well as grant 09PRE2060795 from the American Heart Association (VDV). We thank Elliot Elson, Benjamin Filas, and Yunfei Shi for helpful discussions.

References

References

- M. Abramoff, P. Magalhães, and S. Ram. Image processing with imagej. *Biophotonics international*, 11(7):36–42, 2004.
- M. T. Abreu-Blanco, J. M. Verboon, and S. M. Parkhurst. Cell wound repair in drosophila occurs through three distinct phases of membrane and cytoskeletal remodeling. *J. Cell Biol.*, 193(3):455–464, May 2011.
- D. Ambrosi, G. A. Ateshian, E. M. Arruda, S. C. Cowin, J. Dumais, A. Goriely, G. A. Holzapfel, J. D. Humphrey, R. Kemkemer, E. Kuhl, J. E. Olberding, L. A. Taber, and K. Garikipati. Perspectives on biological growth and remodeling. *J Mech Phys Solids*, 59(4):863–883, Apr. 2011.
- S. S. An and J. J. Fredberg. Biophysical basis for airway hyperresponsiveness. *Can. J. Physiol. Pharmacol.*, 85(7):700–714, July 2007.
- G. B. Arfken and H. J. Weber. *Mathematical Methods for Physicists*. Academic Press, New York, sixth edition, 2005.
- R. Bellairs and M. Osmond. *The Atlas of Chick Development*. Elsevier, New York, second edition, 2005.
- R. Bellairs, D. R. Bromham, and C. C. Wylie. The influence of the area opaca on the development of the young chick embryo. *J Embryol Exp Morphol*, 17(1):195–212, Feb. 1967.
- W. M. Bement, A. L. Miller, and G. von Dassow. Rho gtpase activity zones and transient contractile arrays. *Bioessays*, 28(10):983–993, Oct. 2006.
- H. A. Benink and W. M. Bement. Concentric zones of active RhoA and Cdc42 around single cell wounds. *J. Cell Biol.*, 168(3):429–39, Jan 2005.
- H. Bortier, S. Vandeveld, and L. C. Vakaet. Mechanism of closure of experimental excision-wounds in the bare upper layer of the chick blastoderm. *Int J Dev Biol*, 37(3):459–466, Sept. 1993.
- J. Brock, K. Midwinter, J. Lewis, and P. Martin. Healing of incisional wounds in the embryonic chick wing bud: characterization of the actin purse-string and demonstration of a requirement for Rho activation. *J. Cell Biol.*, 135(4):1097–107, Nov 1996.
- G. T. Charras, M. Coughlin, T. J. Mitchison, and L. Mahadevan. Life and times of a cellular bleb. *Biophys. J.*, 94(5):1836–1853, Mar. 2008.
- A. G. Clark, A. L. Miller, E. Vaughan, H.-Y. E. Yu, R. Penkert, and W. M. Bement. Integration of single and multicellular wound responses. *Curr. Biol.*, 19(16):1389–1395, Aug. 2009.
- J. F. Colas and G. C. Schoenwolf. Towards a cellular and molecular understanding of neurulation. *Dev Dyn*, 221(2):117–145, June 2001.
- G. W. Conrad, J. A. Bee, S. M. Roche, and M.-A. Teillet. Fabrication of microscapels by electrolysis of tungsten wire in a meniscus. *J Neurosci Meth*, 50:123–127, 1993.
- J. V. Cordeiro and A. Jacinto. The role of transcription-independent damage signals in the initiation of epithelial wound healing. *Nat Rev Mol Cell Bio*, 14(4):249–262, Apr. 2013.
- L. A. Davidson, A. M. Ezin, and R. Keller. Embryonic wound healing by apical contraction and ingression in *Xenopus laevis*. *Cell Motil. Cytoskeleton*, 53(3):163–76, Nov 2002.
- J. A. Davies. *Mechanisms of Morphogenesis: The creation of biological form*. Elsevier, 2005.
- S. Deguchi, T. Ohashi, and M. Sato. Tensile properties of single stress fibers isolated from cultured vascular smooth muscle cells. *J Biomech*, 39(14):2603–2610, 2006.
- V. S. Deshpande, R. M. McMeeking, and A. G. Evans. A model for the contractility of the cytoskeleton including the effects of stress-fibre formation and dissociation. *P R Soc A*, 463(2079):787–815, 2007.
- M. A. England and S. V. Cowper. Wound healing in the early chick embryo studied by scanning electron microscopy. *Anat Embryol*, 152(1):1–14, Dec. 1977.
- M. A. England and A. Lawson. Natural wound formation: endodermal responses in experimental primary neural induction in the chick embryo. *Anat Rec*, 236(4):710–720, Aug. 1993.
- M. A. England and J. Wakely. Scanning electron microscopy of the development of the mesoderm layer in chick embryos. *Anat Embryol*, 150(3):291–300, May 1977.
- B. A. Filas, A. Oltean, S. Majidi, P. V. Bayly, D. C. Beebe, and L. A. Taber. Regional differences in actomyosin contraction shape the primary vesicles in the embryonic chicken brain. *Phys Biol*, 9(6):066007, Dec. 2012.
- B. Forster, D. Van De Ville, J. Berent, D. Sage, and M. Unser. Complex wavelets for extended depth-of-field: a new method for the fusion of multichannel microscopy images. *Microsc. Res. Tech.*, 65(1-2):33–42, Sept. 2004.
- Y. C. Fung. *Biomechanics: Mechanical Properties of Living Tissues*. Springer, New York, 1993.
- N. Gorfinkiel and G. B. Blanchard. Dynamics of actomyosin contractile activity during epithelial morphogenesis. *Curr. Opin. Cell Biol.*, 23(5):531–539, Oct. 2011.

- V. Hamburger and H. L. Hamilton. A series of normal stages in the development of the chick embryo. 1951. *J. Morphol.*, 88(1):49–92, 1951.
- J. Humphrey and K. Rajagopal. A constrained mixture model for growth and remodeling of soft tissues. *Math Mod Meth Appl S*, 12(3):407–430, Jan 2002.
- M. S. Hutson and X. Ma. Mechanical aspects of developmental biology: perspectives on growth and form in the (post)-genomic age. *Phys Biol*, 5(1):015001, 2008.
- M. S. Hutson, Y. Tokutake, M.-S. Chang, J. W. Bloor, S. Venakides, D. P. Kiehart, and G. S. Edwards. Forces for morphogenesis investigated with laser microsurgery and quantitative modeling. *Science*, 300(5616):145–9, Apr 2003.
- M. S. Hutson, J. Veldhuis, X. Ma, H. E. Lynch, P. G. Cranston, and G. W. Brodland. Combining laser microsurgery and finite element modeling to assess cell-level epithelial mechanics. *Biophys. J.*, 97(12):3075–3085, Dec. 2009.
- A. Jacinto, W. Wood, T. Balayo, M. Turmaine, A. Martinez-Arias, and P. Martin. Dynamic actin-based epithelial adhesion and cell matching during *Drosophila* dorsal closure. *Curr. Biol.*, 10(22):1420–1426, Nov. 2000.
- A. Jacinto, A. Martinez-Arias, and P. Martin. Mechanisms of epithelial fusion and repair. *Nat. Cell Biol.*, 3(5):E117–23, May 2001.
- K. E. Kasza and J. A. Zallen. Dynamics and regulation of contractile actin-myosin networks in morphogenesis. *Curr. Opin. Cell Biol.*, 23(1):30–38, Feb. 2011.
- R. Kaunas and S. Deguchi. Multiple roles for myosin II in tensional homeostasis under mechanical loading. *Cel. Mol. Bioeng.*, 4(2):182–191, 2011.
- D. P. Kiehart. Wound healing: The power of the purse string. *Curr. Biol.*, 9(16):R602–5, Aug. 1999.
- D. P. Kiehart, C. G. Galbraith, K. A. Edwards, W. L. Rickoll, and R. A. Montague. Multiple forces contribute to cell sheet morphogenesis for dorsal closure in *drosophila*. *J. Cell Biol.*, 149(2):471–490, Apr. 2000.
- V. Klepeis, A. Cornell-Bell, and V. Trinkaus-Randall. Growth factors but not gap junctions play a role in injury-induced ca^{2+} waves in epithelial cells. *J. Cell Sci.*, 114(23):4185–4195, 2001.
- A. Lawson and M. England. Surface ectodermal wound healing in the chick embryo. *J Anat.*, 192:497–506, Jan 1998.
- A. T. Layton, Y. Toyama, G.-Q. Yang, G. S. Edwards, D. P. Kiehart, and S. Venakides. *Drosophila* morphogenesis: tissue force laws and the modeling of dorsal closure. *HFSP J*, 3(6):441–60, Dec 2009.
- T. Lecuit, P.-F. Lenne, and E. Munro. Force generation, transmission, and integration during cell and tissue morphogenesis. *Annu. Rev. Cell Dev. Biol.*, 27:157–184, Nov. 2011.
- R. Levayer and T. Lecuit. Biomechanical regulation of contractility: spatial control and dynamics. *Trends Cell Biol*, 22(2):61–81, Feb. 2012.
- H. Lodish, A. Berk, P. Matsudaira, C. A. Kaiser, M. Krieger, M. P. Scott, S. L. Zipursky, and J. Darnell. *Molecular Cell Biology*. W.H. Freeman and Company, New York, fifth edition, 2004.
- L. Lu, S. J. Oswald, H. Ngu, and F. C. P. Yin. Mechanical properties of actin stress fibers in living cells. *Biophys. J.*, 95(12):6060–6071, Dec. 2008.
- V. Lubarda and A. Hoger. On the mechanics of solids with a growing mass. *Int J Solids Struct*, 39(18):4627–4664, 2002.
- V. A. Lubarda. Constitutive theories based on the multiplicative decomposition of deformation gradient: Thermoelasticity, elastoplasticity, and biomechanics. *Appl. Mech. Rev.*, 57(2):95–108, 2004.
- X. Ma, H. E. Lynch, P. C. Scully, and M. S. Hutson. Probing embryonic tissue mechanics with laser hole drilling. *Phys Biol*, 6(3):036004, 2009.
- C. A. Mandato and W. M. Bement. Contraction and polymerization cooperate to assemble and close actomyosin rings around *Xenopus* oocyte wounds. *J. Cell Biol.*, 154(4):785–97, Aug 2001.
- M. M. Mareel and L. C. Vakaet. Wound healing in the primitive deep layer of the young chick blastoderm. *Virchows Arch B Cell Pathol*, 26(2):147–157, Dec. 1977.
- A. C. Martin. Pulsation and stabilization: contractile forces that underlie morphogenesis. *Dev Biol*, 341(1):114–125, May 2010.
- A. C. Martin, M. Kaschube, and E. F. Wieschaus. Pulsed contractions of an actin-myosin network drive apical constriction. *Nature*, 457(7228):495–499, Jan. 2009.
- P. Martin and J. Lewis. Actin cables and epidermal movement in embryonic wound healing. *Nature*, 360(6400):179–83, Nov 1992.
- P. Martin and S. M. Parkhurst. Parallels between tissue repair and embryo morphogenesis. *Development*, 131(13):3021–34, Jul 2004.
- T. Matsumoto and K. Nagayama. Tensile properties of vascular smooth muscle cells: bridging vascular and cellular biomechanics. *J Biomech*, 45(5):745–755, Mar. 2012.
- J. McCluskey and P. Martin. Analysis of the tissue movements of embryonic wound healing—DiI studies in the limb

- bud stage mouse embryo. *Dev Biol*, 170(1):102–14, Jul 1995.
- A. Menzel and E. Kuhl. Frontiers in growth and remodeling. *Mechanics Research Communications*, 42:1–14, June 2012.
- R. A. Moreno-Rodriguez, E. L. Krug, L. Reyes, L. Villavicencio, C. H. Mjaatvedt, and R. R. Markwald. Bidirectional fusion of the heart-forming fields in the developing chick embryo. *Dev Dyn*, 235(1):191–202, Jan. 2006.
- J. J. Muñoz, K. Barrett, and M. Miodownik. A deformation gradient decomposition method for the analysis of the mechanics of morphogenesis. *J Biomech*, 40(6):1372–1380, 2007.
- J. D. Murray. *Mathematical Biology II: Spatial Models and Biomedical Applications*. Springer-Verlag, New York, third edition, 2003.
- J. D. Murray and G. F. Oster. Generation of biological pattern and form. *Math Med Biol*, 1(1):51–75, 1984.
- T. Nagai and H. Honda. Computer simulation of wound closure in epithelial tissues: Cell-basal-lamina adhesion. *Physical Review E*, 80(6):061903–, Jan 2009.
- D. A. New. The adhesive properties and expansion of the chick blastoderm. *J Embryol Exp Morphol*, 7:146–164, June 1959.
- A. Ní Annaidh, M. Destrade, M. D. Gilchrist, and J. G. Murphy. Deficiencies in numerical models of anisotropic nonlinearly elastic materials. *Biomech Model Mechanobiol*, 12(4):781–791, Aug. 2013.
- L. Olsen, J. A. Sherratt, and P. K. Maini. A mechanochemical model for adult dermal wound contraction and the permanence of the contracted tissue displacement profile. *J. Theor. Biol.*, 177(2):113–28, Nov 1995.
- G. P. Radice. The spreading of epithelial cells during wound closure in *Xenopus* larvae. *Dev Biol*, 76(1):26–46, Apr 1980.
- A. Ramasubramanian and L. A. Taber. Computational modeling of morphogenesis regulated by mechanical feedback. *Biomech Model Mechanobiol*, 7(2):77–91, 2008.
- A. Ramasubramanian, K. S. Latacha, J. A. Benjamin, D. A. Voronov, A. Ravi, and L. A. Taber. Computational model for early cardiac looping. *Ann Biomed Eng*, 34(8):1355–1369, Jan 2006.
- M. Rauzi and P. Lenne. Cortical forces in cell shape changes and tissue morphogenesis. *Curr Top Dev Biol*, 95: 93–144, 2011.
- H. J. Ray and L. Niswander. Mechanisms of tissue fusion during development. *Development*, 139(10):1701–1711, Apr. 2012.
- M. J. Redd, L. Cooper, W. Wood, B. Stramer, and P. Martin. Wound healing and inflammation: embryos reveal the way to perfect repair. *Philos Trans R Soc Lond, B, Biol Sci*, 359(1445):777–84, May 2004.
- E. Rodriguez, A. Hoger, and A. McCulloch. Stress-dependent finite growth in soft elastic tissues. *J Biomech*, 27(4): 455–467, Jan 1994.
- A. Rodriguez-Diaz, Y. Toyama, D. L. Abravanel, J. M. Wiemann, A. R. Wells, U. S. Tulu, G. S. Edwards, and D. P. Kiehart. Actomyosin purse strings: renewable resources that make morphogenesis robust and resilient. *HFSP J*, 2(4):220–37, Aug 2008.
- A. Sadosky and F. Y. M. Wan. The elastodynamics of embryonic epidermal wound closure. *Stud Appl Math*, 118 (4):365–395, Jan 2007.
- J. A. Sherratt, P. Martin, J. D. Murray, and J. Lewis. Mathematical models of wound healing in embryonic and adult epidermis. *IMA J Math Appl Med Biol*, 9(3):177–96, Jan 1992.
- M. J. Smedley and M. Stanisstreet. Scanning electron microscopy of wound healing in rat embryos. *J Embryol Exp Morphol*, 83:109–117, Oct. 1984.
- K. J. Sonnemann and W. M. Bement. Wound repair: toward understanding and integration of single-cell and multicellular wound responses. *Annu. Rev. Cell Dev. Biol.*, 27:237–263, Nov. 2011.
- M. R. Stachowiak and B. O’Shaughnessy. Kinetics of stress fibers. *New J. Phys.*, 10(2):025002, 2008.
- M. Stanisstreet, J. Wakely, and M. A. England. Scanning electron microscopy of wound healing in *xenopus* and chicken embryos. *J Embryol Exp Morphol*, 59:341–353, Oct. 1980.
- J. Stricker, T. Falzone, and M. L. Gardel. Mechanics of the F-actin cytoskeleton. *J Biomech*, 43(1):9–14, Jan. 2010.
- R. Szilard. *Theory and Analysis of Plates*. Prentice-Hall, Englewood Cliffs, NJ, 1974.
- L. A. Taber. Biomechanics of cardiovascular development. *Annu. Rev. Biomed. Eng.*, 3:1–25, Jan 2001.
- L. A. Taber. *Nonlinear Theory of Elasticity: Applications in Biomechanics*. World Scientific, New Jersey, USA, 2004.
- L. A. Taber. Theoretical study of Belousov’s hyper-restoration hypothesis for mechanical regulation of morphogenesis. *Biomech Model Mechanobiol*, 7(6):427–41, Dec 2008.
- L. A. Taber. Towards a unified theory for morphomechanics. *Philos T R Soc A*, 367(1902):3555–3583, Sep 2009.
- S. Timoshenko and J. N. Goodier. *Theory of Elasticity*. McGraw-Hill Book Company, Inc., New York, second edition, 1951.

- J. Tomasek, G. Gabbiani, B. Hinz, C. Chaponnier, and R. Brown. Myofibroblasts and mechano-regulation of connective tissue remodelling. *Nat Rev Mol Cell Bio*, 3(5):349–363, 2002.
- V. Varner and L. A. Taber. On measuring stress distributions in epithelia. In K. Garikipati and E. M. Arruda, editors, *IUTAM Symposium on Cellular, Molecular and Tissue Mechanics*, pages 45–54, New York, 2010. Springer.
- V. D. Varner and L. A. Taber. On integrating experimental and theoretical models to determine physical mechanisms of morphogenesis. *BioSystems*, 109(3):412–419, Sept. 2012a.
- V. D. Varner and L. A. Taber. Not just inductive: a crucial mechanical role for the endoderm during heart tube assembly. *Development*, 139(9):1680–1690, May 2012b.
- V. D. Varner, D. A. Voronov, and L. A. Taber. Mechanics of head fold formation: investigating tissue-level forces during early development. *Development (Cambridge, England)*, 137:3801–3811, Oct 2010.
- V. Vogel and M. Sheetz. Local force and geometry sensing regulate cell functions. *Nat Rev Mol Cell Bio*, 7(4):265–275, 2006.
- D. A. Voronov and L. A. Taber. Cardiac looping in experimental conditions: Effects of extraembryonic forces. *Dev Dyn*, 224(4):413–21, 2002.
- W. Wood, A. Jacinto, R. Grose, S. Woolner, J. Gale, C. Wilson, and P. Martin. Wound healing recapitulates morphogenesis in *Drosophila* embryos. *Nat. Cell Biol.*, 4(11):907–12, Nov 2002.
- K. Woolley and P. Martin. Conserved mechanisms of repair: from damaged single cells to wounds in multicellular tissues. *Bioessays*, 22(10):911–919, 2000.
- M. A. Wozniak and C. S. Chen. Mechanotransduction in development: a growing role for contractility. *Nat Rev Mol Cell Bio*, 10(1):34–43, 2009.
- M. A. Wyczalkowski, Z. Chen, B. A. Filas, V. D. Varner, and L. A. Taber. Computational models for mechanics of morphogenesis. *Birth Defects Res C Embryo Today*, 96(2):132–152, June 2012.
- G. Xu, A. K. Knutsen, K. Dikranian, C. D. Kroenke, P. V. Bayly, and L. A. Taber. Axons pull on the brain, but tension does not drive cortical folding. *J. Biomech. Eng.*, 132(7):071013, July 2010.
- S. Xu and A. D. Chisholm. A gq-ca signaling pathway promotes actin-mediated epidermal wound closure in *c. elegans*. *Curr. Biol.*, 21(23):1960–1967, Dec. 2011.
- E. A. Zamir and L. A. Taber. On the effects of residual stress in microindentation tests of soft tissue structures. *J. Biomech. Eng.*, 126(2):276–83, Apr. 2004a.
- E. A. Zamir and L. A. Taber. Material properties and residual stress in the stage 12 chick heart during cardiac looping. *J. Biomech. Eng.*, 126(6):823–830, Dec. 2004b.
- E. A. Zamir, V. Srinivasan, R. Perucchio, and L. A. Taber. Mechanical asymmetry in the embryonic chick heart during looping. *Ann Biomed Eng*, 31(11):1327–1336, Dec. 2003.

Appendix S. Supplemental Material

Appendix S.1. Parameters for Experimental Wound Area

	1	2	3	4	5	6	Mean \pm SD
c_0 [μm^2]	-160	60.2	459	2110	199	230	483 ± 751
c_1 [μm^2]	7090	5320	4170	5220	4690	8850	5890 ± 1600
c_2 [μm^2]	3000	2440	1780	3350	2430	3550	2760 ± 606
T_1 [sec]	13.5	8.83	9.62	16.1	12.4	13.7	12.4 ± 2.5
T_2 [sec]	186	82.7	111	131	134	195	140 ± 40

Table S1: Parameters for best fit (Eq. 1) to experiment for six circular wounds. Numbers in column header indicate the wound in Fig. 1a; colors match the plot in Fig. 2 for each wound.

Table S1 lists the parameters obtained from a best fit of Eq. (1) to closing trends of six circular wounds (Figs. 1 and 2). Mean parameter values yield area versus time curve against which model results are compared.

Appendix S.2. Implementation Details

We provide here details of coordinate transformations as well as key tensors in matrix form as an aid to understanding and implementation (see also (Taber, 2008)). Our goal is to calculate the stress carried by cells and fibers, $\boldsymbol{\sigma}^c$ and $\boldsymbol{\sigma}^f$ (Eq. 10), given the total deformation \mathbf{F} and growth tensors \mathbf{G}^c and \mathbf{G}^f (Eqs. 19, 22b).

Appendix S.2.1. Coordinate Transforms

Given, for instance, the tensor \mathbf{G}^c whose components are provided in local (i.e., polar or elliptical) coordinates as in Eq. (19), we can obtain the components in Cartesian coordinates using the relation (Taber, 2004)

$$G_{IJ}^c = \mathbf{e}_I \cdot \mathbf{G}^c \cdot \mathbf{e}_J. \quad (\text{S.1})$$

The quantities R and Θ , as well as the dot product between local (\mathbf{e}_α) and Cartesian (\mathbf{e}_A) unit vectors, $e_{A\alpha} \equiv \mathbf{e}_A \cdot \mathbf{e}_\alpha$, can be calculated as,

$$\begin{aligned} R &= \sqrt{X^2 + Y^2}, & \Theta &= \tan^{-1} Y/X, \\ e_{XR} &= \cos(\Theta), & e_{YR} &= \sin(\Theta), \\ e_{X\Theta} &= -\sin(\Theta), & e_{Y\Theta} &= \cos(\Theta), \end{aligned} \quad (\text{S.2})$$

for polar coordinates and

$$\begin{aligned} R &= \text{Re}(\cosh^{-1} \frac{X+iY}{\alpha}), & \Theta &= \text{Im}(\cosh^{-1} \frac{X+iY}{\alpha}), \\ e_{XR} &= \frac{\sinh(R)}{g} \cos(\Theta), & e_{YR} &= \frac{\cosh(R)}{g} \sin(\Theta), \\ e_{X\Theta} &= -\frac{\cosh(R)}{g} \sin(\Theta), & e_{Y\Theta} &= \frac{\sinh(R)}{g} \cos(\Theta), \\ g &= \sqrt{\cosh^2 R \sin^2 \Theta + \sinh^2 R \cos^2 \Theta}, \end{aligned} \quad (\text{S.3})$$

for elliptical coordinates, where α is a real number defined in Appendix A, and with the understanding that for elliptical coordinates $R = \xi$ and $\Theta = \eta$ (see Appendix A). We can thus write \mathbf{G}^c

in Cartesian coordinates as,

$$\begin{bmatrix} G_{XX}^c & G_{XY}^c & 0 \\ G_{YX}^c & G_{YY}^c & 0 \\ 0 & 0 & G_{ZZ}^c \end{bmatrix} = \begin{bmatrix} G_R^c e_{XR}^2 + G_\theta^c e_{X\Theta}^2 & G_R^c e_{XReYR} + G_\theta^c e_{X\Theta eY\Theta} & 0 \\ G_R^c e_{XReYR} + G_\theta^c e_{X\Theta eY\Theta} & G_R^c e_{YR}^2 + G_\theta^c e_{Y\Theta}^2 & 0 \\ 0 & 0 & G_Z^c \end{bmatrix}. \quad (\text{S.4})$$

Appendix S.2.2. Cell Stress

With \mathbf{G}^c expressed in Cartesian coordinates, we can write the elastic deformation gradient tensor \mathbf{F}^{c*} in Cartesian components as,

$$\mathbf{F}^{c*} = \mathbf{F} \cdot (\mathbf{G}^c)^{-1} = D^{-1} \begin{bmatrix} F_{xX} G_{YY}^c - F_{xY} G_{XY}^c & F_{xY} G_{XX}^c - F_{xX} G_{XY}^c & 0 \\ F_{yX} G_{YY}^c - F_{yY} G_{XY}^c & F_{yY} G_{XX}^c - F_{yX} G_{XY}^c & 0 \\ 0 & 0 & D^2 F_{zZ} \end{bmatrix}, \quad (\text{S.5})$$

with

$$D = G_{XX}^c G_{YY}^c - (G_{XY}^c)^2, \quad (\text{S.6})$$

and find the cell strain invariants as

$$I_1^* = \text{tr} [(\mathbf{F}^{c*})^T \cdot \mathbf{F}^{c*}] = (F_{xX}^{c*})^2 + (F_{xY}^{c*})^2 + (F_{yX}^{c*})^2 + (F_{yY}^{c*})^2 + (F_{zZ}^{c*})^2, \quad (\text{S.7})$$

$$I_3^* = (\det \mathbf{F}^{c*})^2 = [(F_{xX}^{c*} F_{yY}^{c*} - F_{xY}^{c*} F_{yX}^{c*}) F_{zZ}^{c*}]^2. \quad (\text{S.8})$$

We calculate W^c from Eq. (11) and obtain the first Piola-Kirchoff stress tensor \mathbf{P}^c by numerical differentiation as,

$$\mathbf{P}^c = \frac{J}{J^{c*}} \frac{\partial W^c}{\partial \mathbf{F}^T} = \frac{J}{J^{c*}} \begin{bmatrix} \frac{\partial W^c}{\partial F_{xX}} & \frac{\partial W^c}{\partial F_{yX}} & 0 \\ \frac{\partial W^c}{\partial F_{xY}} & \frac{\partial W^c}{\partial F_{yY}} & 0 \\ 0 & 0 & \frac{\partial W^c}{\partial F_{zZ}} \end{bmatrix}. \quad (\text{S.9})$$

Finally, the cell Cauchy stress is obtained as,

$$\boldsymbol{\sigma}^c = J^{-1} \mathbf{F} \cdot \mathbf{P}^c. \quad (\text{S.10})$$

Appendix S.2.3. Fiber Stress

The fiber elastic stretch ratio λ^{f*} , given by Eq. (12), can be calculated (using Eqs. 18, 22b) as,

$$\lambda^{f*} = \frac{\sqrt{C_{\Theta\Theta}}}{G^f}, \quad (\text{S.11})$$

where $C_{\Theta\Theta}$ is the $\mathbf{e}_\Theta \mathbf{e}_\Theta$ component of $\mathbf{C} = \mathbf{F}^T \cdot \mathbf{F}$. We calculate fiber stress by analytical differentiation and write the first Piola-Kirchoff fiber stress components in local coordinates as

$$\mathbf{P}^f = \frac{2\mu_f J}{G^f J^{f*}} \left(1 - (\lambda^{f*})^{-3}\right) \left(F_{r\Theta}^{f*} \mathbf{e}_\Theta \mathbf{e}_r + F_{\theta\Theta}^{f*} \mathbf{e}_\Theta \mathbf{e}_\theta\right). \quad (\text{S.12})$$

This quantity is then transformed into Cartesian Cauchy stress components as described previously, and the total stress $\boldsymbol{\sigma}$ carried by the tissue is given by Eq. (17).

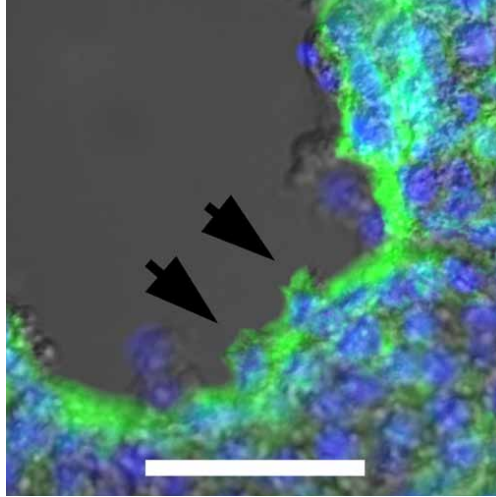


Figure S1: Detail of actin staining in Fig. 4e (endoderm, fixed 1 min after wounding) with cells (gray), nuclei (blue), and actin (green). Arrows indicate lamellipodia; scale bar 50 μm .

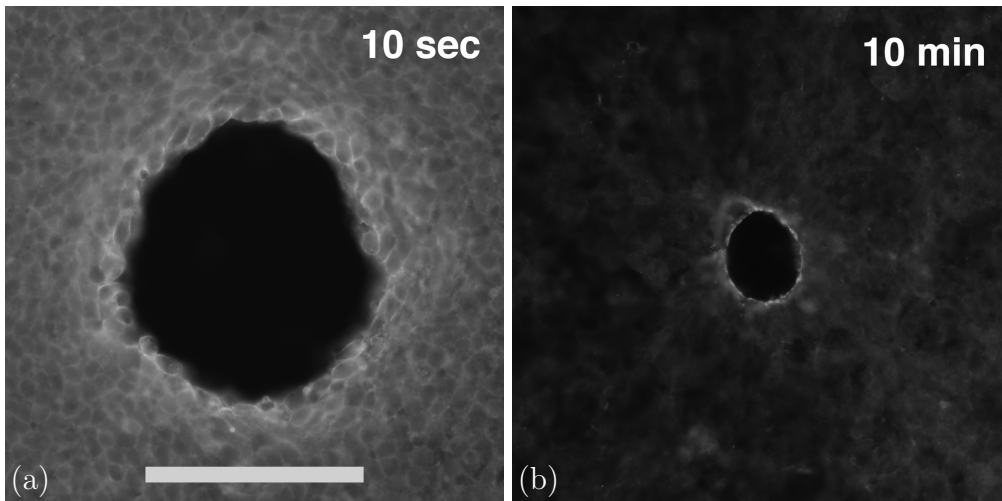


Figure S2: Fluorescence images of ectoderm near circular wound stained for phosphorylated myosin light chain (pMLC) at given times post wounding. Scale bar 100 μm .

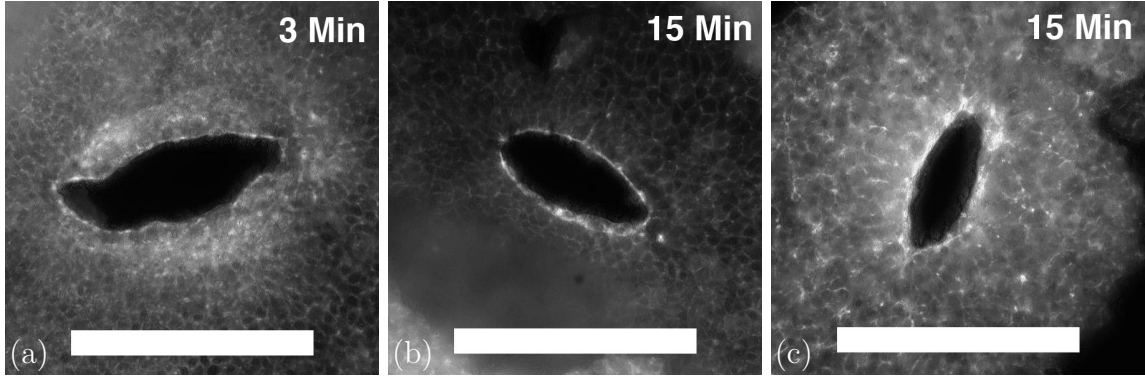


Figure S3: Fluorescence images of elliptical wounds stained for actin at given times after wounding. (a,b) ectoderm; (c) endoderm. Scale bars $200\mu\text{m}$. Panels b and c are same wound. Images have been processed with Extended Depth of Field ImageJ plugin (Forster et al., 2004). Both the cell and fiber rings are visible at 3 minutes, and by 15 minutes a well developed fiber ring is present in both the endoderm and ectoderm.

Appendix S.3. Actin and Myosin Staining

Fluorescent staining for actin at one minute after wounding (Fig. S1) illustrates the formation of the actin purse string and the presence of lamellipodia. Staining for phosphorylated myosin light chain (pMLC) at different times after wounding (Fig. S2) yields distributions similar to those for actin (Fig. 4). These results indicate that pMLC co-localizes with actin in the thick and thin rings, and demonstrate that these structures are actively contractile.

Cell and fiber rings around elliptical wounds are similar to those around circular wounds. Figure S3, shows actin distribution around elliptical wounds at 3 and 15 minutes after wounding. Three minutes after wounding both cell and fiber rings are visible, and at 15 minutes a well developed fiber ring is visible in both germ layers.

Appendix S.4. Stress and Displacement

Circular and elliptical wounds differ primarily in that stress concentrations are more intense along the major axis of the ellipse (Fig. S4, S5, S7). Along both axes, at $t = 0$ the radial stress σ_r is zero at the wound boundary and increases with distance, converging to σ_B some distance away. However, the increase is very sharp along the major axis and much more gradual along the minor one. Similarly, the circumferential stress at $t = 0$ has a value about 70 times greater than σ_B at the wound border along the major axis, while it decreases to less than half of σ_B along the minor axis. Otherwise, contraction of cells and fibers changes the stress distribution in a manner broadly similar to that observed for the circular wound (Sec. 6.3). Figures S6 and S8 plot the tissue displacement relative to the reference (b_0) configuration for circular and elliptical wounds, respectively. In both cases the largest displacement occurs inside of the cell region.

Appendix S.5. Parameter Sensitivity Studies

Differences in membrane pre-stress can explain the initial variations in the healing behavior observed in elliptical wounds. Fig. S9 plots the major and minor radii of both experimental and model elliptical wounds. The initial opening of elliptical wounds is driven by an increase in the minor radius, a behavior which is reproduced by the model for low values of σ_B (see Sec. 6.4).

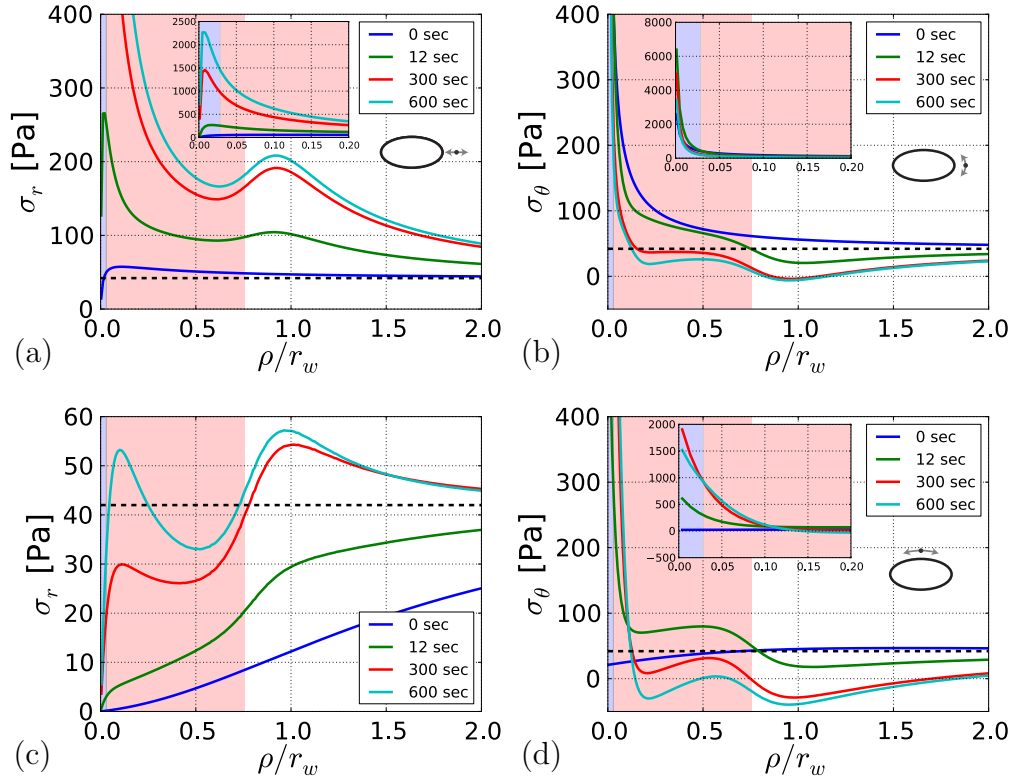


Figure S4: Epithelial membrane stress in the vicinity of elliptical wound. Icons indicate position (along minor or major axis for elliptical wound), and stress component (radial σ_r , circumferential σ_θ). Distance from wound edge in the reference configuration is given in multiples of the circular wound radius r_w , and the fiber and cell regions are indicated with blue and red shading, respectively (see Fig. 7). Far from the wound both stress components approach the far-field value $\sigma_B = 42$ Pa, indicated by black dashed line.

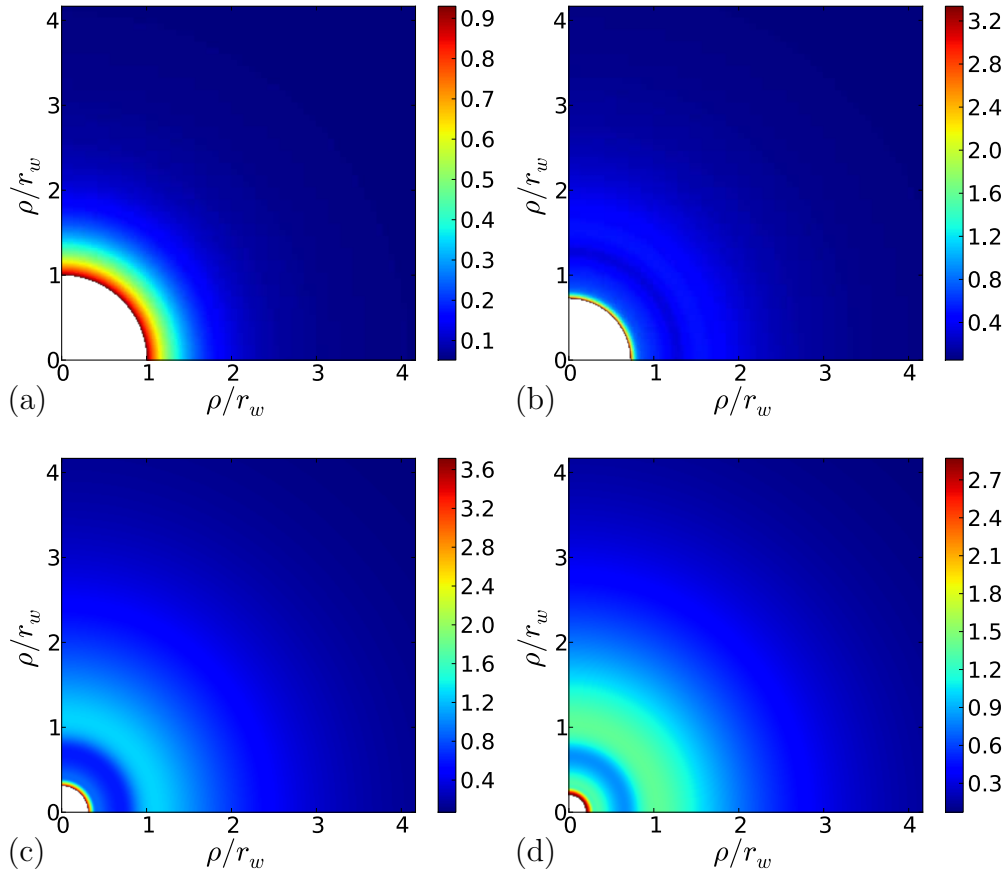


Figure S5: Stress around closing circular wound. Logarithm of Von Mises stress plotted for $t=0, 12, 300,$ and 600 seconds in panels a-d, respectively.

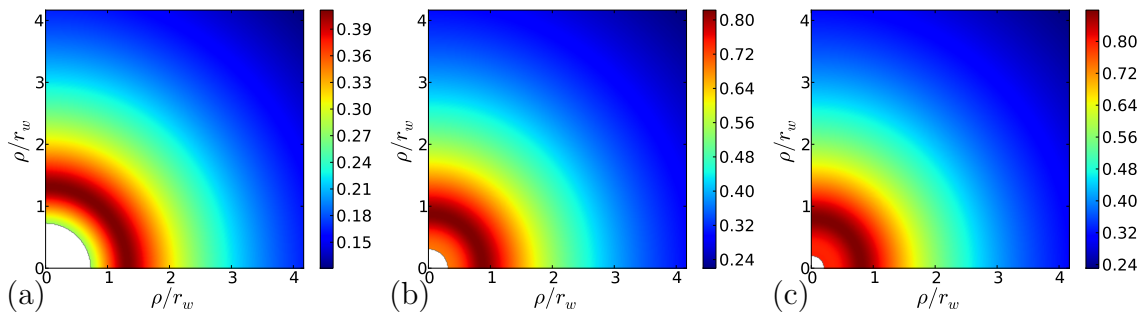


Figure S6: Displacement around closing circular wound relative to the reference ($t=0$) configuration for $t=12, 300,$ and 600 seconds in panels a-c, respectively. Displacement and distance are relative to circular wound radius r_w .

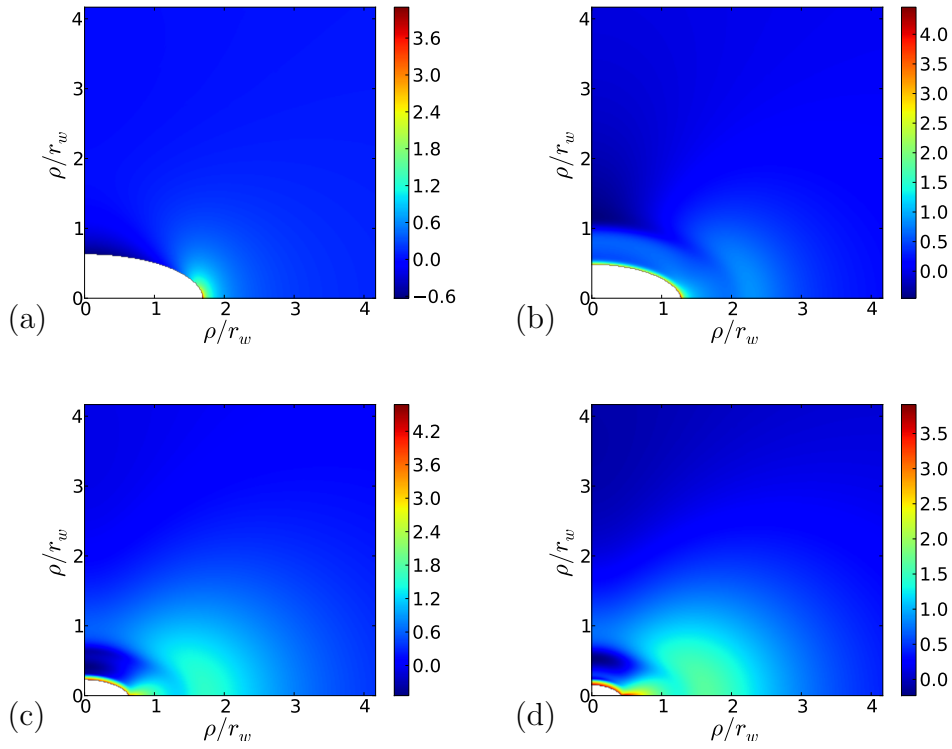


Figure S7: Stress around closing elliptical wound. Logarithm of Von Mises stress plotted for $t=0, 12, 300,$ and 600 seconds in panels a-d, respectively.

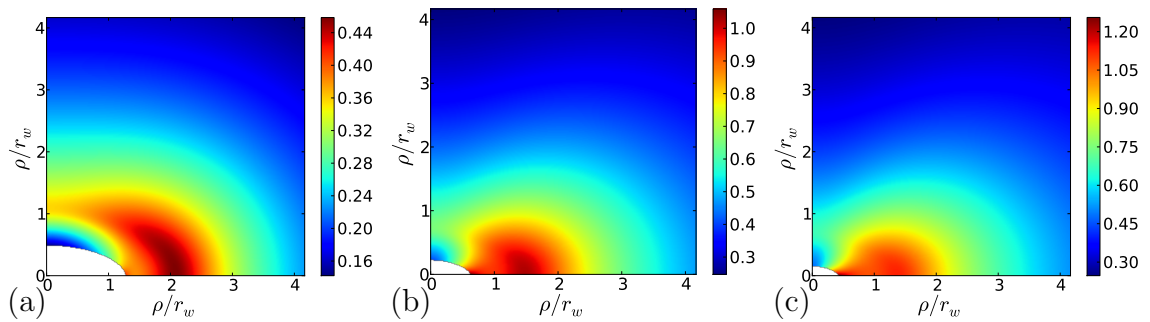


Figure S8: Displacement around closing elliptical wound relative to the reference ($t=0$) configuration for $t=12, 300,$ and 600 seconds in panels a-c, respectively. Displacement and distance are relative to circular wound radius r_w .

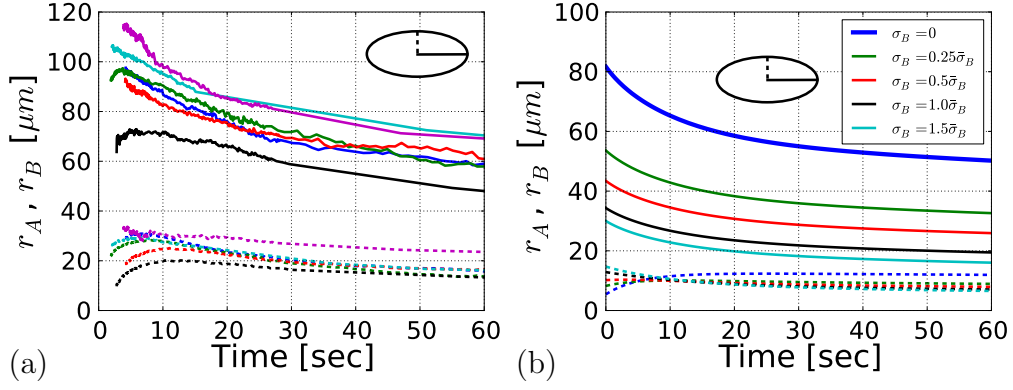


Figure S9: Major and minor radii of elliptical wounds in initial stages of closing. Solid and dashed curves represent major and minor radii, respectively, as indicated by ellipse icons. (a) Radii of experimental wounds. Colors represent individual experiments (data from Fig. 3). (b) Radii of model wounds, with colors indicating boundary tension σ_B , data from Fig. 11.

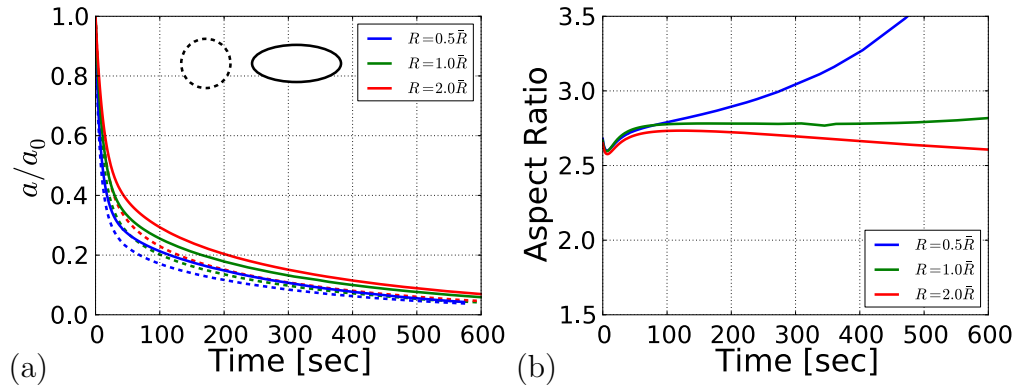


Figure S10: Wound area and aspect ratio (AR) with varying initial area (same σ_B). Dashed and solid curves, correspond to circular and elliptical wounds, respectively, as indicated by icons. Undeformed wound radii (R_w for circular wound, R_A and R_B for elliptical) are varied relative to nominal values (Table 2). Decreasing wound size increases effective width of fiber and cell rings, and results in slightly faster wound closing.

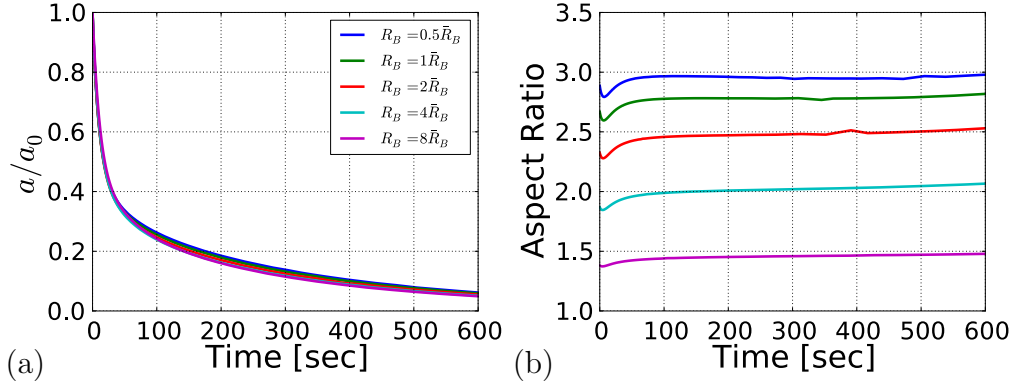


Figure S11: Area and aspect ratio (AR) of model elliptical wounds with varying initial AR. The minor radius in undeformed configuration R_B is varied relative to nominal value (Table 2), i.e., $R_B = 0.5\bar{R}_B$ specifies a wound with increased AR, and a circular wound is equivalent to $R_B \simeq 15\bar{R}_B$. Wound geometry variation is reflected mainly in initial AR and has little effect on relative area or AR trends.

To evaluate the role of wound size and shape on the rate of wound closure, we varied the initial wound size and aspect ratio. With other parameters unchanged, a smaller wound implies proportionately wider cell and fiber contractile rings. The model predicts that smaller wounds close more quickly, particularly in the initial phase of healing where cell contraction dominates (Fig. S10a). The aspect ratios of smaller wounds increase somewhat more than those of larger wounds in the second, fiber-driven phase of wound healing (Fig. S10b), an effect which is analogous with the result of Fig. 8c. In general, however, qualitative aspects of wound closure tend to be relatively insensitive to wound size. This is broadly consistent with experimental observations, where we find that wounds much larger than those considered here will typically heal, albeit much more slowly.

Changing the elliptical wound geometry by modifying the minor radius yields negligible changes in the relative rate of wound closure, and predictable variation in the aspect ratio (Fig. S11). Thus, neither the wound size nor shape has a strong effect on wound behavior, and at least for the value of σ_B under consideration, circular and elliptical wounds behave similarly. This result also supports our approximation of a linear incision, which can be considered an elliptical wound of infinite aspect ratio, by an elliptical wound of an aspect ratio $AR=15$ (Section 5.7.1).

The dynamics of wound closure are quite sensitive to the value of the prestretch F_0^{f*} , as illustrated in Fig S12a. Parameter sets other than those listed in Table 3 can reproduce the experimental circular wound trends, as shown in Fig. S12b

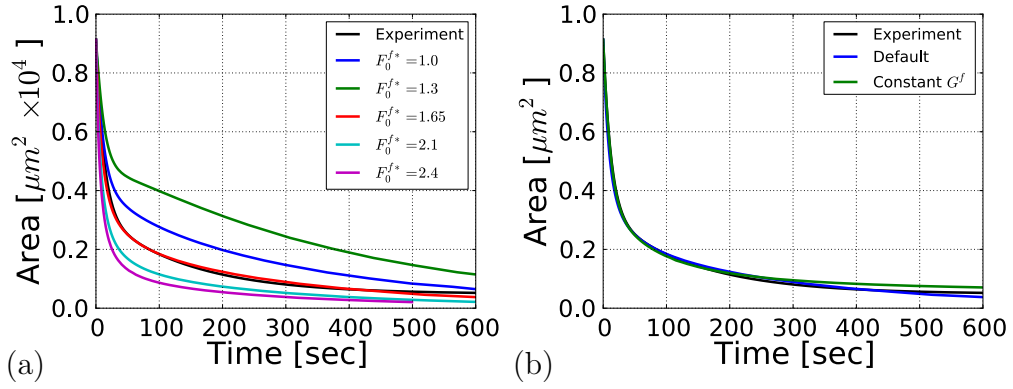


Figure S12: Effects of parameter variation on model behavior. (a) Effect of prestretch F_0^{f*} on circular wounds, with all other parameters as in Table 3. F_0^{f*} has a strong effect on wound healing behavior. (b) Comparison circular wound experiment and model results for two different parameter sets. “Default” parameters correspond to those in Table 3. For “Constant G^f ” parameters, $G_1^f = 1$ (no fiber contraction) with $\tau_\phi = 20$ min and $F_0^{f*} = 3.1$. Results are essentially indistinguishable given the natural variation in wound behavior.